UNIVERSITY OF THESSALY
SCHOOL OF ENGINEERING
DEPARTMENT OF MECHANICAL ENGINEERING

Diploma Thesis

Microscopic Analysis of H13 Tool Steel Produced by SLM: Influence of Process Parameters

By

Christos V. Chorinos

Submitted in partial fulfillment of the requirements for the degree of Diploma in Mechanical Engineering at the University of Thessaly

2025

Approved by the members of the Thesis Committee

First Member (Supervisor)

Dr. Helen Kamoutsi

Lab teaching staff

Department of Mechanical Engineering, University of Thessaly

Second Member (Co-supervisor)

Prof. Gregory N. Haidemenopoulos

Professor of Physical Metallurgy

Department of Mechanical Engineering, University of Thessaly

Third Member

Prof. Emmanouil Bouzakis

Associate Professor of Manufacturing Processes

Department of Mechanical Engineering, University of Thessaly

Date approved: October 07, 2025

Acknowledgements

I would like to express my sincere gratitude to my thesis supervisor, Dr. Helen Kamoutsi, for her valuable guidance and assistance throughout the course of this work. Her advice during the writing process and her expertise in the experimental part of this thesis greatly contributed to its completion.

Furthermore, I am grateful for my collaboration with Professor Gregory Haidemenopoulos, who introduced me to the field of physical metallurgy through his course. I would also like to thank Professor Emmanouil Bouzakis, member of the examination committee of this thesis, for the honor of evaluating my work.

Above all, I would like to thank my family, without whom I would not be who I am today and would not have achieved what I have accomplished. In addition, I wish to express my gratitude to all my friends, and especially to Dimitris, Christos, and Kleanthis, for their support and everything they have offered me throughout this journey. Finally, from the bottom of my heart, I would like to thank Eirini for her selfless love and support.

Sincerely,

Christos Chorinos

October 2025, Volos

Abstract

Selective Laser Melting (SLM) enables the fabrication of complex metal components, yet its wider industrial application is hindered by process-induced defects such as porosity, cracking, and residual stresses—especially in tool steels like H13. This study aims to investigate the influence of process parameters, particularly volumetric energy density (VED), laser power, and scanning speed, as well as the effect of post-processing heat treatment on the microstructure, porosity, and hardness of SLM-manufactured H13 specimens. Six samples were produced with varying process parameters, three of which underwent quenching in ambient air followed by double tempering at 580 °C for 2 hours. Microscopy (optical and SEM), porosity analysis, and hardness measurements were used to characterize the samples. Results showed that as-built specimens exhibited defects such as lack of fusion, pores, and cracks, with higher scan speeds contributing to incomplete fusion. Heat treatment improved microstructural uniformity and hardness, with the best results (600.1 HV and 4.32% porosity) achieved in the specimen processed at the highest VED (135 J/mm^3). Overall, the study confirms that appropriate parameter selection combined with heat treatment can significantly enhance the mechanical integrity and applicability of H13 steel parts produced by SLM, offering valuable insights for high-performance tooling applications.

Table of Contents

LIST OF FIGURES

LIST OF TABLES

1 INTRODUCTION

1.1 Problem Definition

Additive manufacturing (AM) is an innovative method, which allows the production of complex three-dimensional parts directly from CAD models. AM has its roots in the 1980s, when it first emerged through the work of Hideo Kodama, who initially applied it to polymer materials. Over time, the process evolved and was subsequently adapted for use with metallic materials as well, leading to the development of various techniques, including Selective Laser Melting (SLM). SLM follows a layer-by-layer technology where layers of metallic powder are melted and fused together by a high power-density laser.

This innovatory technique is followed by plethora of advantages, some of which are the following:

(a) direct manufacturing of metal function parts without intermediate procedures

(b) ability to produce with higher accuracy more complex parts than the pre-existing techniques

(c) higher strength and hardness, supported by existing experimental data

(d) excellent strength to weight ratios

(e) reduced material waste compared to conventional methods.

In addition, due to the ability of forming that type of parts, SLM is widely used in aerospace, automobile industry and even in medical fields when it comes to the design of medical implants. Even though this technique is characterized by enhanced features, it is necessary to define several variables, some of which have not been thoroughly investigated in terms of their influence on the process, let alone the inherent time and cost constraints associated with it. Therefore, it remains a field that could be characterized as unexplored in comparison with all the conventional methods such as casting.

A concise description of SLM process could be the following: a layer of powder measured in micrometers is spread over a pre-existing surface and then melted by a high power-density laser considering a finite cooling rate. The procedure is repeated until the final layer is applied and the component has assumed its final form. An inhomogeneous temperature field is

generated by the high-power-density laser, and its spatial distribution influences the metal's final microstructure. Moreover, the intense temperature fluctuations during these repeated thermal cycles lead to non-equilibrium behavior, deviating from classical equilibrium assumptions, a fact that ultimately affects the mechanical properties of the final product. Therefore, it is evident that the study of this method requires consideration of various fields, including mass and heat transfer, phase transformations, solidification, and both elastic and plastic deformation.

H13 tool steel is a chromium–molybdenum alloy widely recognized for its suitability in both hot and cold work tooling applications. Its ability to retain mechanical strength at elevated temperatures significantly enhances its resistance to thermal fatigue cracking—an issue typically caused by cyclic thermal loading in hot working environments. Due to this unique combination of high toughness and thermal fatigue resistance, H13 has become the most extensively utilized tool steel in hot work operations. Furthermore, the alloy's high toughness and dimensional stability during heat treatment make it a reliable choice for cold work tooling as well. In such contexts, H13 offers improved hardenability—especially across larger cross-sectional areas—and exhibits better wear resistance when compared to conventional alloy steels such as AISI 4140.

1.2 Thesis Objective and Outline

Although extensive research has been conducted in the field of Additive Manufacturing (AM), and in particular Selective Laser Melting (SLM), its industrial adoption remains relatively limited. This is primarily due to ongoing challenges related to processing time, production cost, build size constraints, and ensuring the full functionality of the manufactured components. In this context, the present study aims to contribute to a deeper understanding of the process by investigating how key processing parameters—namely volumetric energy density (VED), laser power, and scanning speed—as well as the subsequent tempering heat treatment, affect the final microstructure and hardness of H13 tool steel. Through this approach, the study seeks to shed light on the relationships between process conditions and material performance, providing useful insights for optimizing SLM applications in industrial settings.

2 LITERATURE REVIEW-THEORY

2.1 Tools steels and H13 steel

Tool steels constitute a specific category of iron-based alloys with a high alloying content, which provides them with high hardness, wear resistance, and thermal stability. H13 tool steel is a common example of this category, particularly within the subcategory of hot-work tool steels, where tools are subjected to high thermal and mechanical loads, such as extrusion dies, die-casting molds, and hot-forming tools (***Figure 2.1***). [1–3]

H13 is a tool steel in which carbide-forming elements such as vanadium (V), molybdenum (Mo), and chromium (Cr) contribute to its ability to retain hardness at elevated temperatures and to resist softening during service. The final microstructure of a wrought product consists of high-hardness martensite with fine carbides, while post-heat treatments optimize its mechanical behavior.

Figure 2.1: Aluminum extrusion die steel H13 [adapted from 4]

2.2 Effect of alloying elements on H13

H13 steel consists of five alloying elements, which are the following: Carbon (C), Chromium (Cr), Silicon (Si), Molybdenum (Mo) and Vanadium (V). Each one plays a crucial role on the development of the microstructure and on the mechanical properties of the metal.

Carbon is the most important and common element in steels, because it contributes in its strength, hardness and hardenability of the steel. Hardenability is the ability of a steel to harden in depth during quenching, that is, the ease with which austenite transforms into martensite throughout the cross-section of the component. A steel with high hardenability can form martensite even in low cooling rates and at greater depth from the surface. Moreover, the presence of alloying elements contributes to higher hardenability, because they delay carbon diffusion as well as the development of ferrite, pearlite and bainite, allowing martensite to form without the necessity of extremely fast cooling rates[5].

Silicon (Si) prevents the creation of oxides and inclusions (FeO, MnO), which degrade steel's mechanical properties, because it captures the oxygen present following this reaction[5]:

$$Si+O_2 \rightarrow SiO_2$$

Chromium (Cr) is carbide former. In the low Cr/C ratio range, only alloyed cementite (Fe, Cr)3C forms. If the Cr/C ratio rises, chromium carbides (Cr, Fe)7C3 or (Cr, Fe)23C6 or both, would appear. Chromium increases hardenability, corrosion and oxidation resistance of the steel while it improves high-temperature strength. Chromium carbides are hard and wear-resistant and increase the edge-holding quality, which is the ability of a blade or cutting tool material to maintain a sharp edge during use without becoming dull quickly. Complex chromium–iron carbides slowly go into solution in austenite, therefore, a longer time at temperature is necessary to allow solution to take place before quenching is accomplished[5].

Molybdenum (Mo) is a pronounced carbide former. It dissolves slightly in cementite, while molybdenum carbides will form when the Mo content in steel is high enough. Molybdenum can induce secondary hardening during the tempering of the steel and improves the creep strength of low-alloy steels at elevated temperatures. The addition of Mo produces fine-grained steels, increases hardenability, and improves fatigue strength, while increases corrosion resistance[5].

Vanadium (V) is a very strong carbide former. It dissolves in austenite, strongly increasing hardenability, but the undissolved vanadium carbides decrease hardenability. Vanadium is a grain refiner, and imparts strength and toughness. Vanadium provides a very strong secondary hardening effect on tempering; therefore, it raises hot-hardness. Moreover, it increases fatigue strength and improves notch sensitivity. Vanadium increases wear resistance, edge-holding quality, and high-temperature strength[5].

For all the reasons mentioned above, it is clear that each alloying element plays an important role in the microstructure and the mechanical behavior of H13 steel.Table ***2.1*** summarizes the properties of the alloying elements, focusing on their effect on H13 steel.

Table 2.1 Effect of alloying elements on H13 steel

Alloying Element	Role in H13 Steel
Carbon (C)	Increases strength, hardness, and hardenability.
Silicon (Si)	Prevents oxides and inclusions. Increases hardenability, wear resistance, yield strength, elastic limit, and scale resistance.
Chromium (Cr)	Carbide former. Increases hardenability, corrosion/oxidation resistance, and high-temperature strength. Enhances wear resistance and edge-holding quality.
Molybdenum (Mo)	Carbide former. Induces secondary hardening during tempering. Improves creep strength, corrosion resistance, fatigue strength, and produces fine-grained steels.
Vanadium (V)	Strong carbide former. Grain refiner, increases strength, toughness, wear resistance, fatigue strength, hot hardness, and edge-holding quality. Provides secondary hardening on tempering.

2.3 Quenching and Martensitic Transformation

The first processing step after the production of this steel is austenitizing. The steel is heated to a temperature range between 1000-1050°C, where a homogenous austenitic phase predominates. After isothermal holding, the steel undergoes quenching. Quenching is a strengthening treatment which refers to cooling from the temperature range of the solid solution at such a rate that transformations in the primary and bainite ranges are suppressed and martensite is formed. In this state, steels are characterized by the greatest hardness. To provide a required cooling rate during quenching, various cooling media and methods are employed. Examples of commonly used quenching media include water, oil and air.

Martensite forms from austenite through a displacive transformation, where there is a perfect match between the initial and final lattice positions. The rapid cooling prevents the diffusion

of carbon atoms, trapping them in interstitial positions within the body-centered tetragonal (BCT) martensitic lattice. In essence, martensite is formed by a shear transformation of the parent matrix (austenite). The kinetics of the transformation and the morphology of martensite are governed by the strain energy, which is characterized by a strong shear component. This transformation is the key mechanism for achieving the high hardness of the steel after quenching. The transformation from austenite to martensite proceeds athermally as the temperature is reduced below Ms until the martensite finish temperature (Mf) is reached, at which point 100% martensite is expected. However, if the Mf temperature is below room temperature, then some austenite may be retained if only cooled to room temperature. The Ms temperature is affected from the alloying elements of the steel. Elements like C, N, Ni, Mn lower the Ms, as well as Cr, Mo, Al, Si, W, and V, which are not austenite stabilizers, also cause a decrease in the Ms temperature, since they strengthen the solid solution in austenite, thereby hindering the dislocation motion required for the formation of the martensitic nucleus. Thus, to overcome this resistance, a greater chemical driving force is required, and consequently the Ms temperature is reduced. The influence of the above elements in the value of the Ms can be described with this empirical relationship:

$$M_s(°C) = 539-463C-30.4Mn-17.7Ni-12.1Cr-7.5Mo$$

where the alloying elements are given in wt.% [6].

Because the martensite transformation occurs through a shear mechanism and without diffusion, the morphology of martensite is mostly lath-, lenticular or plate-like. Although martensite is characterized by its great hardness, it is also very brittle. For the above reason, quenching is usually followed by a heat treatment called tempering, where steel becomes more ductile while losing a small amount of hardness.

2.4 Selective Laser Melting of the H13 tool steel

2.4.1 Introduction to SLM and H13

Additive manufacturing encompasses a variety of technologies for producing components in an additive, layer-wise fashion. These technologies can broadly be grouped into one of seven

major classes based on the mechanism in which each layer is formed: photopolymerization, extrusion, sheet lamination, beam deposition, direct write and printing, powder bed binder jet printing, and powder bed fusion[7]. This review is focused on the last of these where a focused energy beam is used to fuse powder particles together on a layer-wise basis. Selective Laser Melting (SLM) is included in powder bed fusion (PBF) category and was developed by Dr. M. Fockele and Dr. D. Schwarze of F & S Stereolithographietechnik GmbH, with Dr. W. Meiners, Dr. K. Wissenbach, and Dr. G. Andres of Fraunhofer ILT to produce metal components from metallic powders[8,9]. Its ability to create precise and complex 3D metal parts with improved mechanical properties and without material waste makes this technology superior to conventional methods. Generally, the essence of manufacturing customized molds/dies makes H13 tool steel very suitable for additive manufacturing[10]. On the other side, SLM also involves many risks related to severe brittleness and scattered distribution of mechanical properties.

2.4.2 Description of the SLM process

The SLM process consists of a series of steps from CAD data preparation to removal of fabricated component from the building platform[8]. Figure 2.2 illustrates the principle of the SLM process and the steps the process can divided into.

The SLM process starts with a CAD model that contains information about the areas to be melted in separate layers. The 3D-CAD volume model is broken down into layers and transferred to the SLM machine. Subsequently, an elevator in the powder reservoir lifts a prescribed dose of powder (***Figure 2.3***) above the level of a base plane and then the powder is layered by a recoating mechanism. The recoating mechanism may consist of a hard scraper, soft squeegee, or roller[11]. The powder layer thickness is typically between 10 and 100 μm[12]. The geometric information of the individual layers is transmitted by a high-power laser beam to the powder bed wherein the regions to contain solid material are scanned under an inert atmosphere (typically carried out in a nitrogen or argon atmosphere with very low oxygen content), leaving a solid layer of the piece to be produced. Lasers in the metal powder bed system are typically fiber lasers with wavelengths in the 1.06–1.08-μm range[12]. Powder particles absorb energy when the high energy laser beam irradiates on the powder bed. After lowering the substrate by one layer thickness, the process steps are repeated until the part is finished[13]. Once the laser scanning process is completed, loose powders are removed from the

building chamber and the component can be separated from the substrate plate manually or by electrical discharge machining (EDM). Besides the data preparation and removal of fabricated component from the building platform, the entire process is automated[8]. In ***Figure 2.4*** there is a schematic diagram of the SLM process described above.

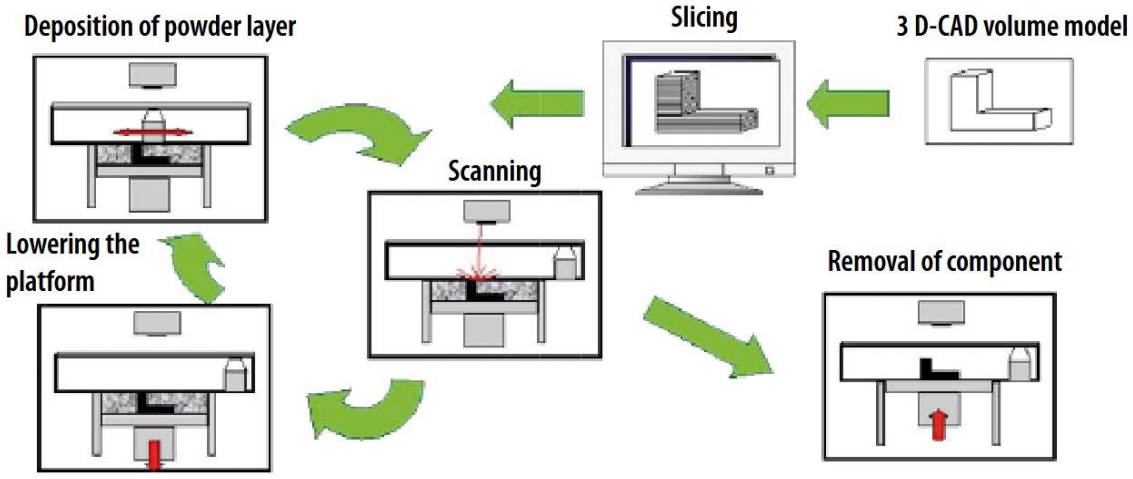

Figure 2.2: Principle of the SLM process [adapted from [9,13]]

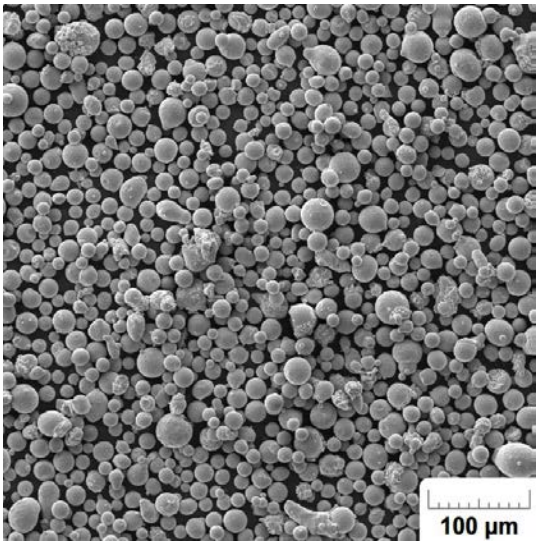

Figure 2.3: SEM picture of H13 tool steel powder [adapted from [14]]

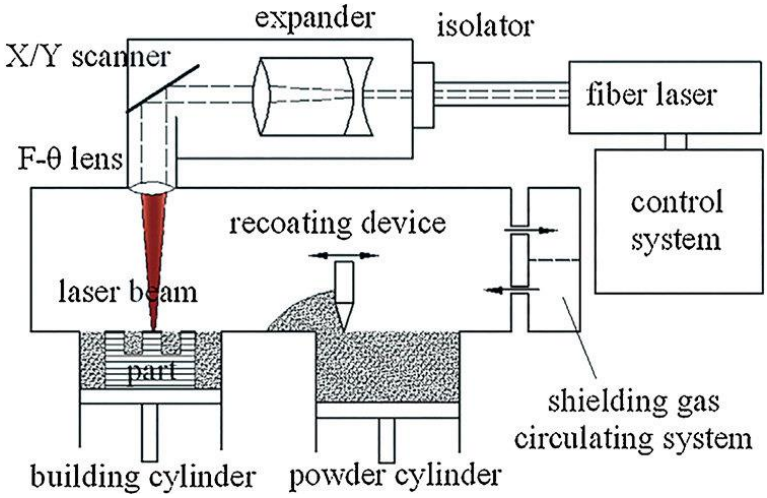

Figure 2.4: A schematic diagram of the SLM procedure [adapted from[15]]

In ***Figure 2.6***, the plane of X-Y, Y-Z and Z-X are shown, from an optical micrograph, for a specimen manufactured with SLM. Each surface of X-Y, Y-Z and Z-X had different shape of microstructure. The scan track can be observed in X-Y plane as shown in the schematic diagram

in ***Figure 2.5***. The melt pool shape can be found well in Y-Z plane. The layering of the powder can be clearly seen in Z-X plane.

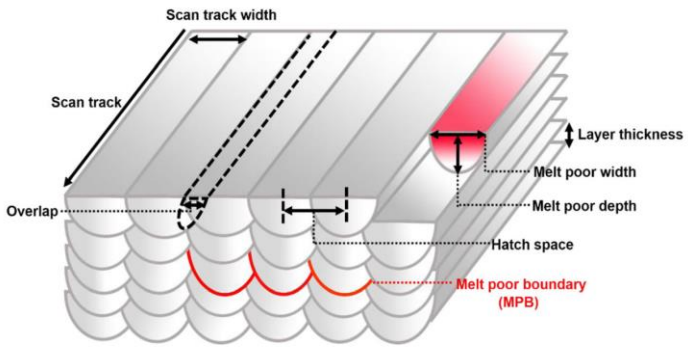

Figure 2.5: A schematic diagram of a scanning strategy in SLM [adapted from [16]***]***

Figure 2.6: Optical micrograph of a typical SLMed specimen in the X-Y, Y-Z, and Z-X planes. [adapted from[17]***]***

A transient temperature field with high temperature and rapid cooling rate is the characteristic of the SLM, which will affect the microstructure and mechanical properties of the specimens[1]. The cooling rates observed in SLM fabricated H13 steels can reach approximately 1.83×10^4 K/s.[18] Hence, suitable combination of laser power, scanning speed, hatch spacing, and layer thickness is essential for SLM processing to successfully build near full-density parts.

2.4.3 Process Parameters of SLM

Selective Laser Melting is a complex method with several process parameters that impact the ultimate quality of the finished parts. There are over fifty parameters that can be placed into one of four categories:

i. Laser and scanning parameters
ii. Powder material properties
iii. Powder bed properties and recoat parameters
iv. Build environment parameters

These can be further classified into controllable parameters that can be manipulated during a build process and predefined parameters that are determined at the start of a build and

remain essentially set throughout the process[12]. In this study the main process parameters are examined below.

2.4.3.1 Laser and Scanning parameters

The core of the SLM procedure is the laser that is used as well as the scanning strategy that the last follows. Therefore, the optimum selection of the laser for different kind of materials and geometries has a vital contribution in the final result. There are many kinds of lasers that can be divided into the solid lasers, gas lasers, liquid lasers, semiconductor lasers, chemical lasers, and excimer lasers[19]. Generally, the lasers needed for selective laser melting are mainly YAG lasers, CO2 lasers, fiber lasers, etc. Moreover, the mode of the laser can be pulsed or continuous. Continuous lasers are the standard in industrial machines, however, pulsed lasers have been demonstrated [20,21] to provide some advantages in preventing cracking or controlling the microstructure of the material[22,23]. The laser expels heat to the powder and melts it until the final product is manufactured. How much power is delivered by the laser is a function of the laser power output (P), the mode of the laser (continuous/pulsed), the area to which the beam energy is applied (spot size), and the amount of time the energy is applied to a given area of the powder bed (scanning speed)[24–26]. The industry standard for SLM machines is the unpolarized IR laser (wavelength of ~1.06 μm). Wavelength and polarization can affect absorptivity and hence these are parameters that are not usually changed throughout SLM processes[27].

The path that the laser follows to melt each layer it is by no means accidental. The scanning strategy of the process affects the heat transfer as well as thermal gradients inside the product and has been observed to determine the resulting properties of the last[28]. Common scanning patterns include hatches in arrays of parallel stripes, contour offset scanning (***Figure 2.7***), partition scanning (***Figure 2.8***), rotary scanning (***Figure 2.9***), spiral line-filling scanning (***Figure 2.10***), scanning line-filling scanning, zig-zagging etc[9,28]. The most common scanning parameter is scan spacing (S_s), which is typically the distance between neighboring passes of the laser[26]. Some degree of overlap between neighboring melt pool areas is typically desired to ensure the material is fully dense and achieves full strength[12]. Yasa et al. proposed sectorial scanning as a scanning strategy for SLM (figure for sectorial scanning strategy). This strategy breaks down a layer into small square grids and neighboring grids are scanned perpendicular to one

another. In ***Figure 2.11*** there is a schematic diagram of this scanning method. They admit that "chessboard" strategy, as it is also known, is able to reduce the residual stresses significantly[8]. Zheng et al.[29] insists that the 67° rotation (***Figure 2.9***) between layers can effectively improve the manufacturing quality and help reduce the roughness accumulated layer by layer during the printing process. When the interlayer rotation is 0°, the laser path of each layer is exactly the same; the molding quality is poor, and the roughness is high.

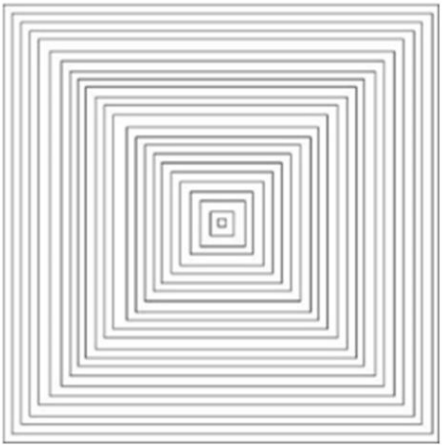

Figure 2.7: Schematic diagram of contour offset scanning [adapted from[9]]

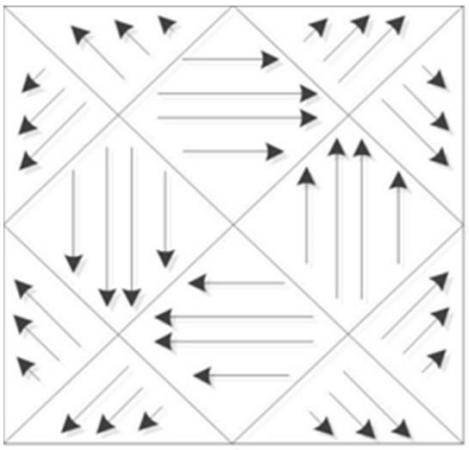

Figure 2.8: Schematic diagram of partition scanning [adapted from[9]]

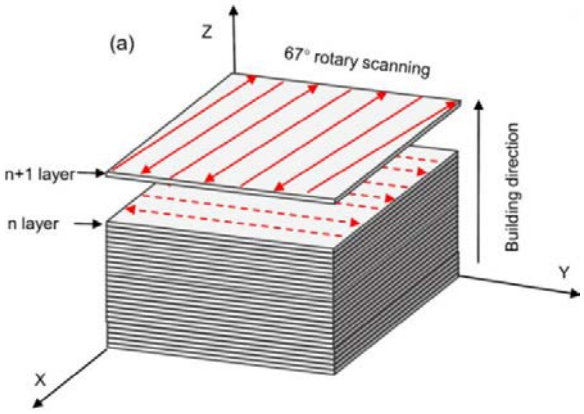

Figure 2.9: Schematic diagram of 67°rotary scanning [adapted from[2]]

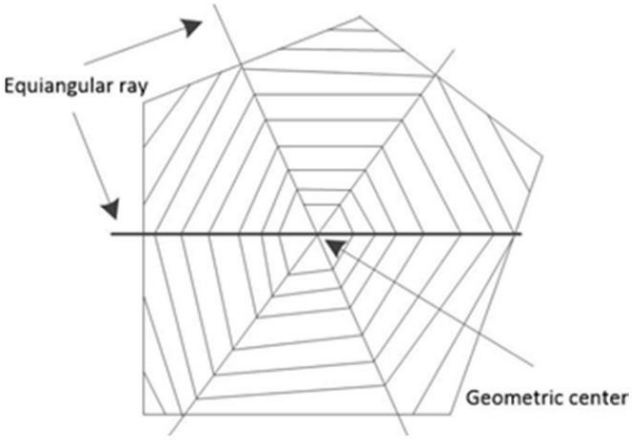

Figure 2.10: Schematic diagram of spiral fill scanning[adapted from[9]]

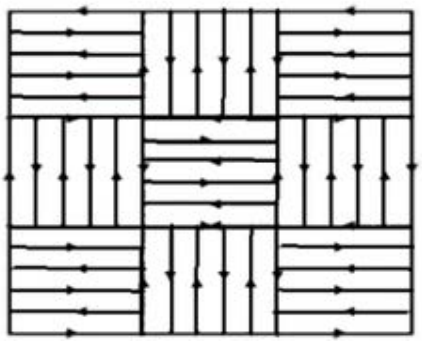

Figure 2.11: Schematic diagram of "chessboard" scanning[adapted from [30]]

2.4.3.2 Powder material properties

2.4.3.2.1 Particle Size Distribution

The product quality of selective laser melting (SLM) is closely related to the powder particle size distribution. Gao et al[9]. found that the small void ratio of the bed, mixed with coarse and fine powders, is beneficial to improve the density of SLM products. However, the fine-grained powder will lead to poor uniformity of powder distribution in SLM equipment, resulting in holes in SLM products. Yap et al. argued that powders with larger particulate sizes result in poor resolution and build tolerance, while smaller powders have the tendency to agglomerate together easily due to van der Waals forces, resulting in poor powder flowability and hence poor powder deposition.

2.4.3.2.2 Absorption of Laser by Materials

One of the integral aspects of laser-material interaction is the absorption of energy by the powder. The absorptance, defined as the ratio of the energy flux absorbed by the material to the energy flux incident upon the material, affects the energy efficiency of the SLM process. It can even determine the feasibility of processing materials with a specific laser[8]. In addition to standard thermophysical properties, the powder particle shape, surface roughness, and size distributions can also be important as these impact light absorption, flowability of the powder during the recoat process, packing of the powder bed, and the uniformity of layers deposited in the recoat process[12].

2.4.4 Microstructure in an SLMed state

After laser powder bed fusion, the as-built microstructure consists predominantly of martensite, retained austenite (RA), and carbides, arranged in a highly segregated cellular/dendritic solidification structure, which promotes the stabilization of approximately 20 vol% RA at the cell walls [1,3,31,32]. This undesirable amount of RA can be transformed during tempering to tempered martensite and carbides[3]. The microstructure for tooling applications typically contains little if any RA to ensure dimensional stability of the finished parts. Furthermore, due to the high cooling rate of H13 steel produced by SLM, the distribution of Cr, Mo, and V during solidification is restrained. Hence strong segregation of those carbide elements is expected, while simultaneously increasing the thermal stability of this unconventional RA [33]. Similarly, due to the rapid cooling, the carbide cannot diffuse in time, which promotes the formation of martensite rather than ferrite.

2.4.5 Microstructure after tempering

Tempering above 600°C, a faster carbide precipitation kinetics leads to the formation of fine and dispersed particles, which promote secondary hardening. As carbide precipitation consumes C, martensite loses tetragonality but retains its lath or plate morphology, being identified as tempered martensite. In this stage, carbides coalesce and martensite laths or plates coarsen. Simultaneously with the evolution of martensite, RA undergoes decomposition. Generally, RA transforms to ferrite or carbides at temperatures above 600-700°C, however in high alloyed steels, it remains stable and transforms to martensite at temperatures ranging from 300 to 350°C, depending on the Ms temperature. Martensite formation is associated to carbide precipitation from austenite during tempering, which consumes C and locally increases the M_s temperature[3]. In conclusion, the final microstructure anticipated after the tempering treatment of the steel is tempered martensite, carbides from secondary hardening and a small percentage of retained austenite, which was not fully dissolved (***Figure 2.12***)[1,3,10,34].

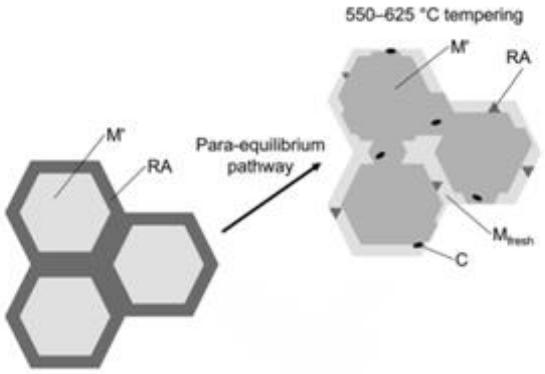

Figure 2.12: A schematic diagram of the transformation of the microstructure before and after tempering [adapted from [3]].

2.5 Defects of the SLM method

Despite the fact that SLM has a lot of advantages and can be widely used in the manufacturing industry, it also presents several defects that can render an SLM-ed product non-functional. Initially it is very important to mention the key process parameters, which are the laser power, the scanning strategy, the hatch space and the layer thickness. These parameters can be explained with the volumetric energy density, VED [J/mm3] as ***Equation 2.1***:

$$E = \frac{Q}{t} = \frac{P}{v * h * t} \qquad \textit{Equation 2.1}$$

where Q is heat input [J/mm^2], t is layer thickness [mm], P is laser power [W], v is laser scan speed [mm/s], and h is hatch space [mm]. Volumetric Energy Density includes many parameters in one value and can be solely used to predict the microstructure, the hardness and other mechanical properties. However, Bertoli et al.[35] found that VED does not capture melt pool physics and therefore cannot be solely used to predict print quality. Changing the values of those parameters can result to different microstructures and properties. The possible defects that can occur during this method are presented more thoroughly below.

2.5.1 Porosity-Low density

Low density is one of the most common defects in AM and specifically in SLM. A relatively high percentage of porosity can result in a degradation of the mechanical properties of the SLM-ed product. Several studies have indicated that there are three main reasons by which these defects are produced. First, gas pores can be formed either due to gas entrapment into the powder particles during the powder atomization process or due to the entrapment of the shielding gas or alloy vapors inside the molten pool (***Figure 2.13*** (b))[36,37]. Second, when laser's power density (P) is very high, deposition or melting may be performed in keyhole mode. Keyholes are very prone to form and collapse, leaving almost spherical voids inside the deposit that consist of entrapped vapor (***Figure 2.13*** (a, b ,c))[38]. Third, inadequate penetration of the molten pool of an upper layer into either the previously deposited layer or the substrate can provoke lack of fusion (LoF) (***Figure 2.13*** (d, e, f)) [38,39].

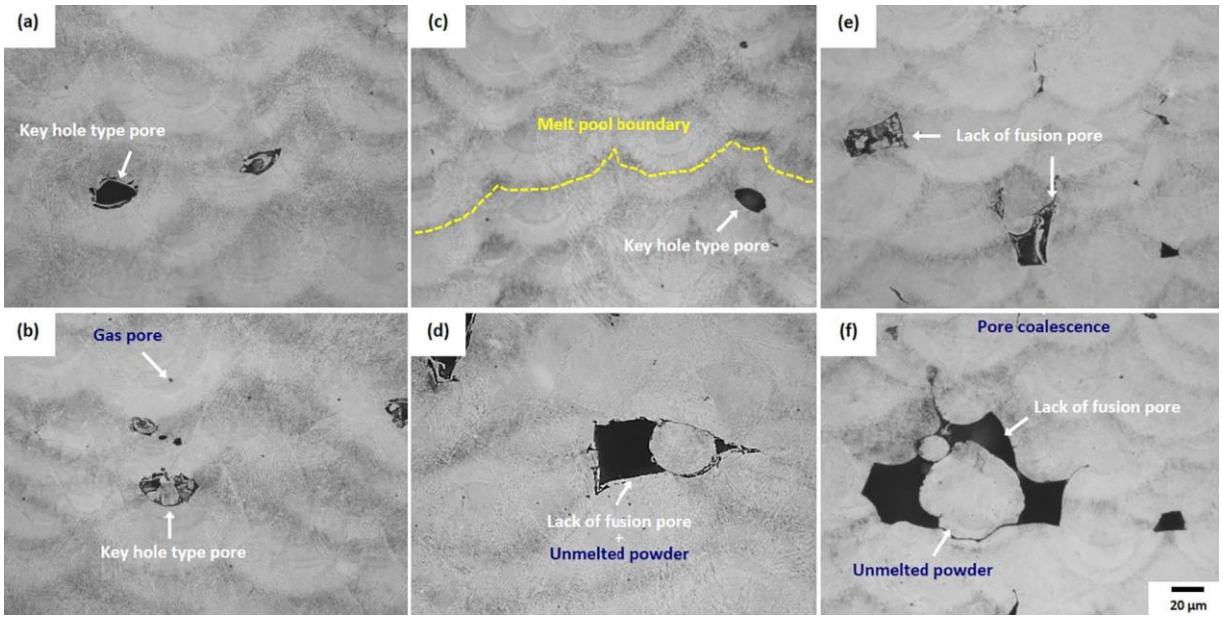

Figure 2.13: Different types of porosity [adapted from[17]]

Several studies have examined the correlation between process parameters, such as VED, scanning speed and strategy, power, and hatch spacing, and the density of the SLM-ed part. Wang et al. [1] proposed that as VED increases up to 60 J/mm^3 , the density also increases. The maximum density is about 99.7%. Moreover, increasing scanning speed with constant laser power, leads to negative effects on the density. They also found that laser remelting can result

to lower porosity on the surface of the specimen and thus to higher density. Finally, it was stated that Hot Isostatic Pressing (HIP) heat treatment proved the relative density the SLMed H13 steel. Katancik et al. reported that decreasing VED leads to lack of fusion (LoF). They also found that highest densities were achieved between 60-120 J/mm^3 (***Figure 2.14***) and post heat treatment doesn't have any effect in porosity. The main topic of this study was to investigate the correlation between VED and LoF at lower energies. They proposed a VED of 760 J/mm^3, with 152W, 100mm/s scanning speed, 50μm layer thickness and 40μm hatch space, as an optimal value for 0.5% porosity. Lei et al.[2] concluded that the maximum relative density reached 99.6% under the optimized process parameters, including P = 230 W, Vs = 800 mm/s and VED = 95.8 J/mm^3. Vele et al.[14] confirmed that to obtain material with a minimal possible porosity for H13 tool steel, VED of at least 100.3 J/mm^3 must be applied. This setup resulted in a porosity of 0.2%. Higher VED does not lead to any further minimization of porosity, while values lower than 87.5J/mm^3 result to a high scatter in values of porosity. Lee et al.[17] studied the porosity as a function of laser scan speed (Figure 2.15). Higher scan speed led to higher porosity. Scanning speeds between 200-400 mm/s resulted to small sized gas pores and keyhole type pores while 800mm/s had unmelted powder with lack of fusion pore, which led to high porosity.

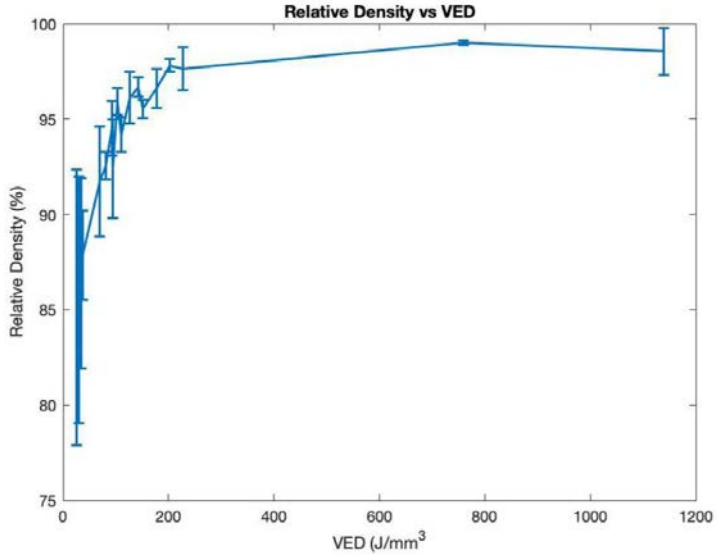

Figure 2.14: Relative density of SLM-manufactured parts vs. VED. [adapted from [34]].

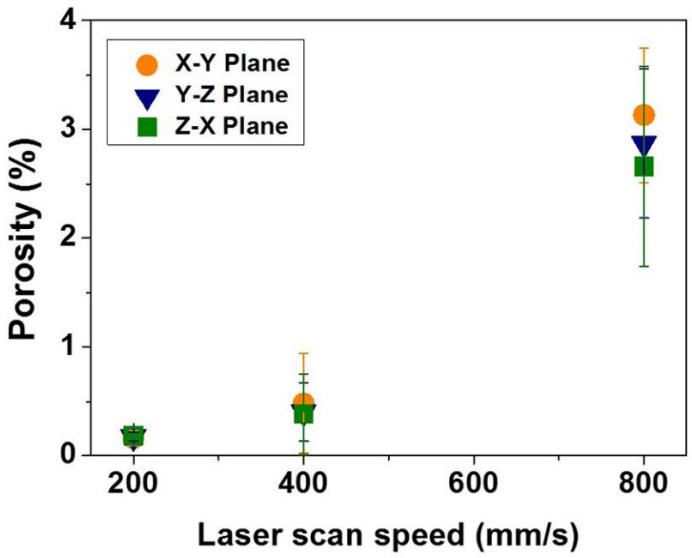

Figure 2.15: Porosity of SLM processed H13 steel as a function of laser scan speed. [adapted from [17]]

2.5.2 Cracks

A very frequent failure in AM processes is cracking. The presence of cracks limits seriously the performance of parts. The main reason for the formation of the cracks are the high thermal stresses that created inside the part, due to the high cooling rates of this method[1,34,38]. The upper layer of solid matrix will expand due to high temperature, while the lower solidified layer will limit this expansion. This makes the upper layer of the substrate produces a significant compressive stress, which may be higher than the yield strength of the material and lead to plastic deformation of the upper layer. When the plastic deformation layer cooling is present, their state is transformed into residual tensile stress. These residual stresses may cause cracking of the part. When the yield strength is attained, the compressive stress causes plastic deformation in the upper layer. In addition, the melted top layer tends to shrink owing to thermal shrinkage. This deformation is again blocked by the lower layer, thus introducing tensile stress into the uppermost layers[1]. In ***Figure 2.17*** there is a schematic diagram of how the thermal stresses are distributed in each layer.

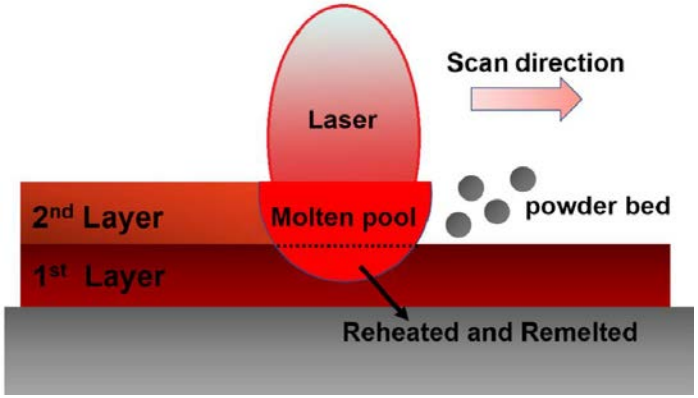

Figure 2.16: Schematic diagram of how the laser affects the layers during SLM [adapted from [1]]

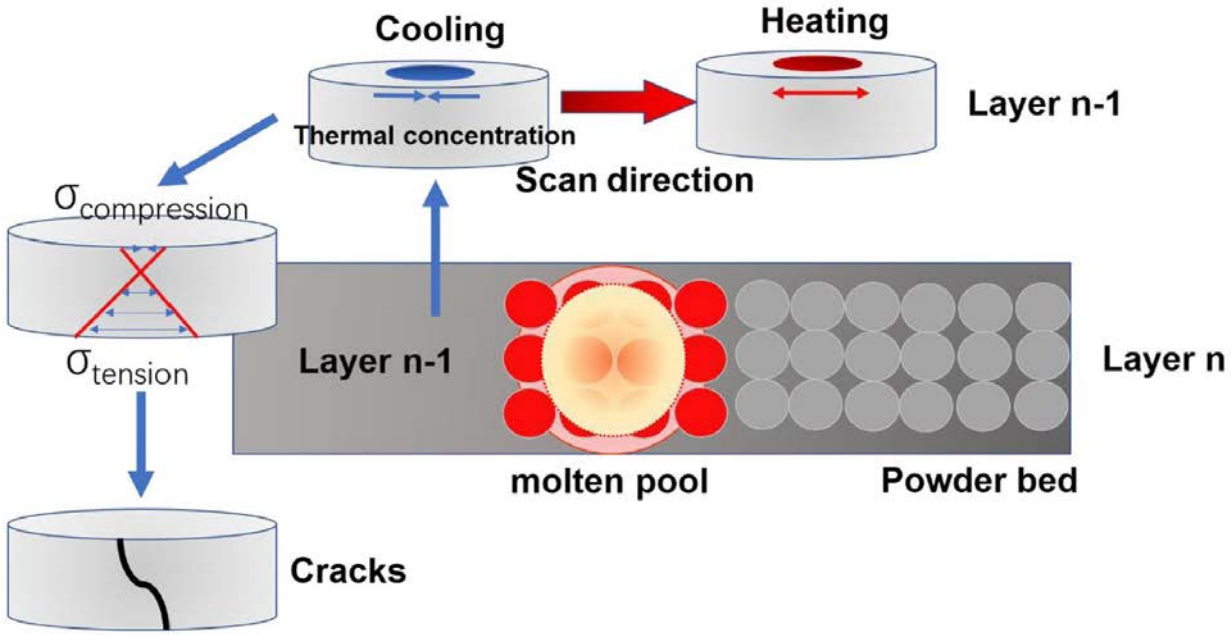

Figure 2.17: Thermal stresses in SLM [adapted from[1]]

Duan et al.[40] observed that most of the cracks produced in H13 samples originate from the side edge of the sample, and propagate along the formed layer to the inside of the sample, and finally terminate at the inside of the sample (***Figure 2.18*** (a, b)). They also argued that during the process of crack propagation, some branched secondary cracks with smaller size are induced near the coarse main cracks to prevent the main cracks from continuing to propagate (***Figure 2.18*** (c). Finally, they stated that the existing pores in the microstructure are more prone to cause some micro-cracks with small size, due to local stress concentration. Katancik et al.[34] observed cracks in the building direction at high VED value. They proposed that preheating the baseplate can be an effective method to reduce residual stresses and eliminate cracking. However, the preheat results to a greater amount of retained austenite in the part, which, regarding quality, is negative, but it enhances fatigue life in certain applications. Lei et al.[2] proposed also to preheat the substrate to eliminate cracking and prevent delamination in AM procedure. Delamination is another type of cracking, which is basically the separation of two consecutive layers, due to residual stresses at the layer interfaces exceeding the yield strength of the alloy (***Figure 2.19***).

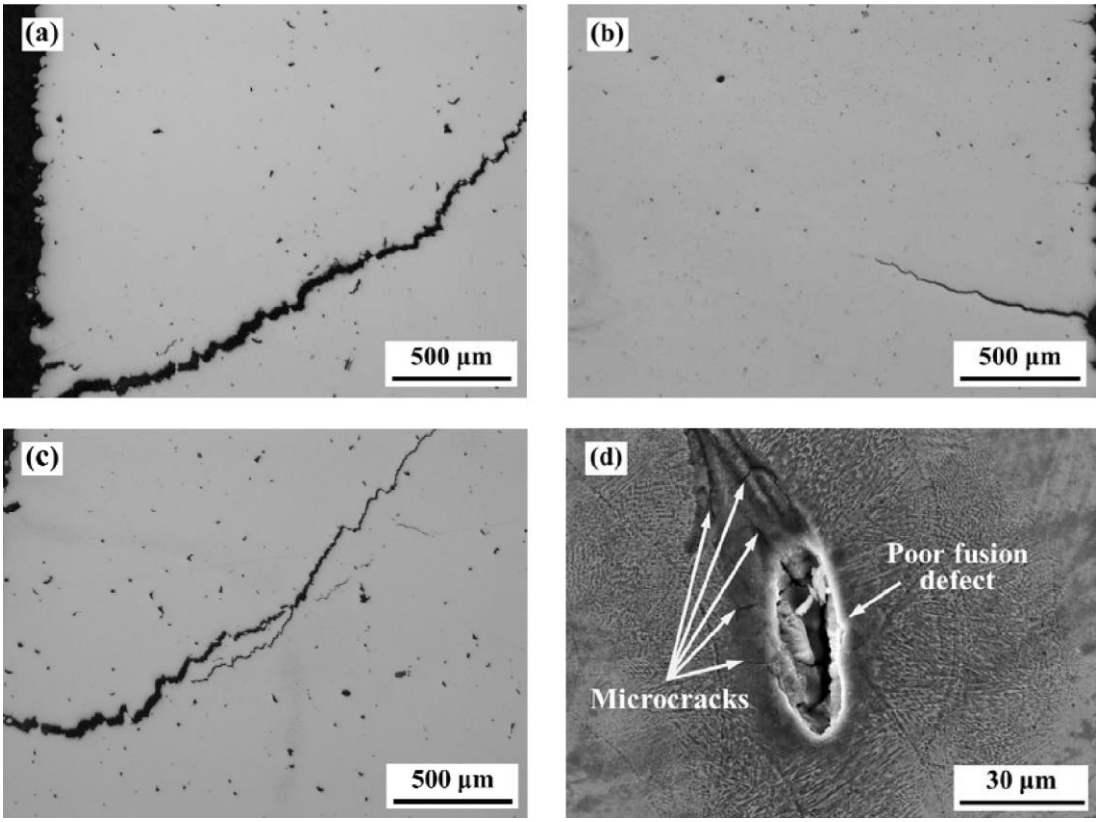

Figure 2.18: OM or SEM images showing different types of cracks [adapted from [40]]

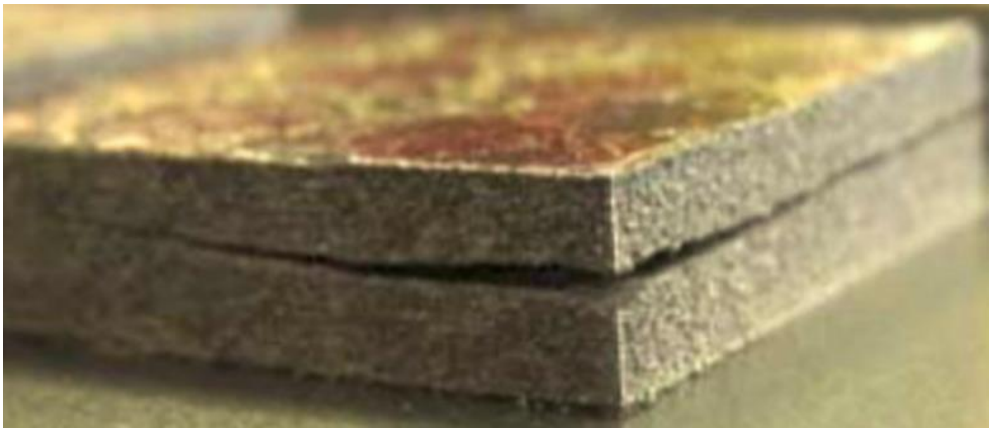

Figure 2.19: Delamination defect in SLM [adapted from [38]]

2.5.3 Rough surface

Surface roughness is one of the most important features of complex geometries produced by AM. Surface roughness is measured using a profilometer or analyzing the surface morphology using SEM. On the surface, the height of a peak or the depth of a valley (f_n) is measured at N locations along the profile length L. Consequently, the average surface roughness (Ra) is calculated using ***Equation 2.2*** as:

$$R_a = \frac{1}{N}\sum_{i=1}^{N}|f_n| \qquad \textit{Equation 2.2}$$

There are two main mechanisms bringing about rough surfaces in additively manufactured parts. "Staircase effect" is one of the mechanisms that finds its roots in the stepped approximation by layers of curved and inclined surfaces in complex geometries[22]. This mechanism is absent in this study, because the specimens do not have curved or inclined surfaces[41]. The second mechanism is the insufficient melting of the powder particles on the bed and balling phenomenon[1,28,41,42]. Gu et al.[42] observed that balling phenomenon is frequently presented in two forms. Using a low laser power gave rise to the first kind of balling phenomenon characterized by significantly coarsened balls possessing inherent structural weakness. A limited amount of liquid formation and a low undercooling degree of the melt due to a low laser input was responsible for its initiation (Figure 2.20). The second kind of balling effect featured by a large number of micrometer-scaled balls on the laser sintered

surface occurred at a high scan speed. Its formation was ascribed to the laser-induced melt splashes caused by a high capillary instability of the melt (Figure 2.21). After research they concluded that increasing the input energy density -achieved by increasing laser power, lowering scan speed, or decreasing powder layer thickness - significantly improved feasibility of alleviating the balling phenomenon.

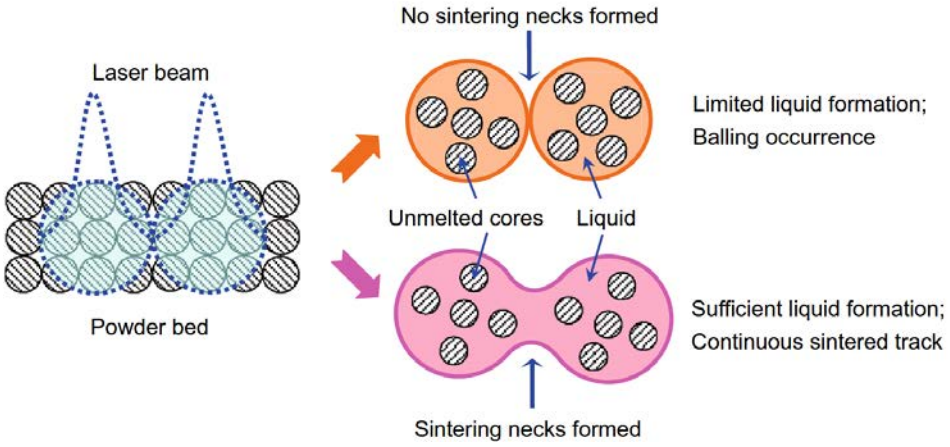

Figure 2.20: Schematic diagram of first kind of balling phenomenon [adapted from[42]]

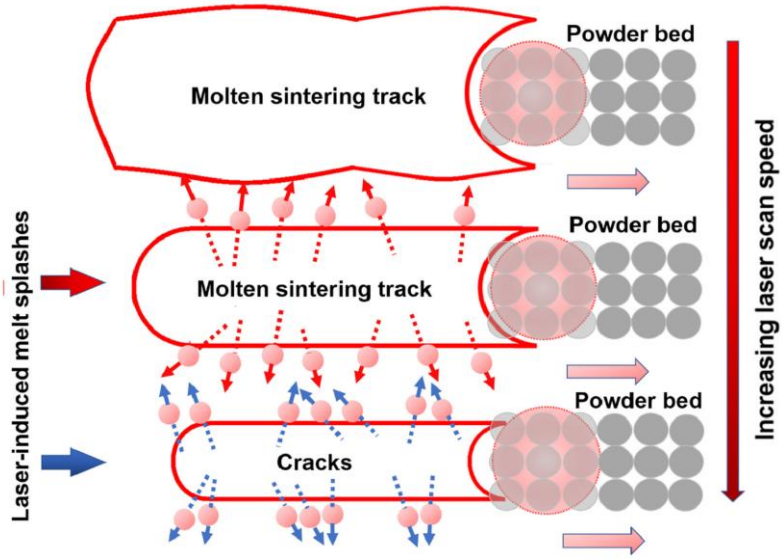

Figure 2.21: Schematic diagram of second kind of balling phenomenon caused be high laser scanning speed [adapted from [1]]

DebRoy et al.[38] proposed that building a part with small layer thickness can effectively reduce the surface roughness. However, it takes more time to build parts with thin layers. Alternative way is to avoid a sharp build orientation angle by properly selecting the building direction for complex parts[43]. DebRoy[38] also pointed out that increasing heat input can completely melt all

the powder particles and reduce the balling phenomenon. However, very high heat input can be detrimental for surface finish due to high thermal stresses and non-uniform solidification rate [44]. Gu et al.[42] concluded that increasing heat input leads to structural refinement and continuity of laser processed materials and thus prevent the occurrence of first kind of balling. They also confirmed that the second kind of balling effect can be eliminated by using a lower scan speed. Narvan et al.[41] conducted several roughness measurements to different specimens manufactured with different process parameters and agreed with the literature that increasing heat input improves surface roughness. More specifically, it was observed that specimens manufactured with 100W laser power consists of high surface roughness, while increasing the heat input to 200-300W clearly resulted to smoother surface. This is explained from the fact that the increase in heat input yields to a wider melt pool causing a better overlap between adjacent scan tracks. Finally, noticed that preheating of 200°C used in this study had no substantial effect on quality of the obtained surfaces. For all the reasons mentioned above, it is clear that surface roughness is a main defect in SLM and must be controlled to prevent failures.

2.5.4 Residual stresses

As mentioned above, many defects such as porosity, cracking and delamination are most often attributed to the same cause, which is residual stresses. An inherent consequence of the deposition of liquid alloy powder on a relatively cooler substrate or prior deposited layers is the steep temperature gradient, thermal strain and residual stresses. These residual stresses not only affect the defects already mentioned, but also deteriorate the fatigue performance and fracture resistance of the fabricated part[38]. Gao et al.[45] identified appropriate strategies to mitigate residual stresses. The substrate preheat temperature, shorter deposition length or scanning in smaller islands, effective deposition strategy such as spiraling-in as against spiraling-out, increase in scanning speed and decrease in layer height were found significant recourses to reduce or mitigate both distortion and residual stresses. Although laser's power and scanning speed have an influence on residual stresses, they also contribute to the size of the melt pool and thus are not suggested as desirable ways to mitigate residual stress. Yan et al.[18] demonstrated that the martensitic transformation that occurs during the SLM of the H13 steel is proposed to be the main contributing factor to the high compressive residual stress

detected. Wang et al.[1] stated that the base plate must to be thick and strong to resist the probable I deformation[18,28,46]. They calculated that the range of residual stress of an SLMed H13 sample is approximately 900–1500 MPa. Besides, the finished parts need to be annealed for 2h in temperature range of 600-650°C to relieve stress[18,47].

3 METHODOLOGY-EXPERIMENTAL

This chapter presents the methodology applied to all specimens in the laboratory in order to obtain accurate and reliable results.

3.1 Material studied and categorization of the specimens

In this diploma thesis, the material under examination is H13 tool-steel. The allowing elements and the chemical composition of the material are presented in ***Table 3.1***.

Table 3.1 Chemical composition of H13 tool steel

Material	C	Cr	Mo	Si	V	Fe
H13 tool steel (wt.%)	0.4	5.25	1.35	1	1	balance

A total of six specimens were produced with SLM for the purposes of this study. The specimens had an approximately cubic geometry with dimensions of 10 × 10 × 10 [mm]. All six of the AM produced samples were made in a 30° Celsius chamber and had 0.025mm layer height, 0.040mm hatching distance and 0.060mm effective beam diameter. The time between each layer was 37.8 seconds. The time required for the formation of a single layer depended on the scanning speed applied and more specifically: (a) 2.5 seconds for the specimens fabricated with a scanning speed of 2000 mm/s and (b) 5 seconds for the specimens fabricated with a scanning speed of 1000 mm/s. Each specimen was manufactured with different process parameters, such as volumetric energy density (VED), power (P) and scanning speed (v). Afterwards, the heat-treated specimens were all austenitized at 1040° Celsius for the duration of one hour and then quenched in ambient air. Three of them then tempered twice in 580° Celsius for two hours. In ***Table 3.2*** are presented the specimens along with the values of their process parameters.

Table 3.2 Process parameters of the different AM samples

AM produced	VED [J/mm^3]	Power [W]	Scanning speed [mm/s]
As-Built 1	68	135	2000
As-Built 2	100	100	1000
As-Built 3	135	135	1000
Heat treated 1	68	135	2000
Heat treated 2	100	100	1000
Heat treated 3	135	135	1000

3.2 Metallographic analysis procedure

The metallographic analysis, that was followed in the laboratory, consisted of grinding, polishing, stereoscopy, optical microscopy, hardness testing and porosity measurements. The aim of this analysis was to understand how process parameters as well as tempering treatment affect the microstructure, the hardness and the porosity of the specimen. In the subsection below, the preparation of the specimens will be analyzed thoroughly.

3.2.1 Specimen preparation

In order to place a specimen on the microscope and obtain necessary data, there are certain steps required before proceeding. Firstly, the specimen undergone grinding using silicon carbide (SiC) abrasive papers with the grit pattern of 80, 220, 400, 800, 1000 and in the presence of water as lubricant to keep the temperature steady and avoid any tempering with the respective thermal process. Subsequently, the specimen undergone polishing, where diamond paste of 3μm was used on a short-nap cloth for polishing, again in the presence of a water-based lubricant. When the proper surface was obtained, an etching solution was applied for 30 seconds on each side to prepare the specimens for observation in the optical microscope, distinguishing the different phases in the microstructure. The solution used was Nital 5% which contained 95% ethanol and 5% nitric acid. This procedure was followed on both transverse and parallel to the scanning direction side of the specimens so that both faces would be examined because of the inhomogeneity in the microstructure from the process.

3.2.2 Metallography preparation of the specimens

The metallographic examination consisted of stereoscopy, optical microscopy and SEM. More specifically, all six specimens were examined in two out of their three planes both on a stereoscope and a microscope. The stereoscope used was Leica WILD M3Z, the microscope was the Leitz Aristomet microscope and the SEM was the JEOL JSM-5310 Scanning Microscope. The specimens were analyzed at magnifications ranging from ×6 to ×1000, allowing the collection of data from a general overview to more detailed observations. The target of this procedure was to investigate the microstructure of each specimen in relation to the process parameters and the heat treatments it had undergone.

3.2.3 Microhardness measurements

Microhardness testing was performed in Vickers scale, with a load of 300g using the Wilson Instrument 402 MVD Vickers and Knoop Tester. Thoroughly, a total of 16 measurements were carried out across different areas on both sides of each specimen – 8 along the building direction and 8 along the horizontal direction on each side. The mean value of the measurements for each sample was then calculated.

3.2.4 Porosity measurements

Porosity calculations were carried out using the ImageJ software. Initially, microscopic images were taken before etching (***Figure 3.1***), in order to obtain a clearer view of porosity and cracking. These images were then imported into ImageJ, and by adjusting the threshold, the porosity percentage was calculated (***Figure 3.2***).

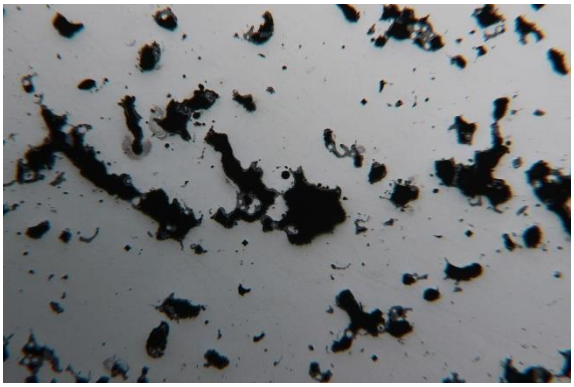

Figure 3.1Original microscopic image of a specimen showing visible porosity (x50)

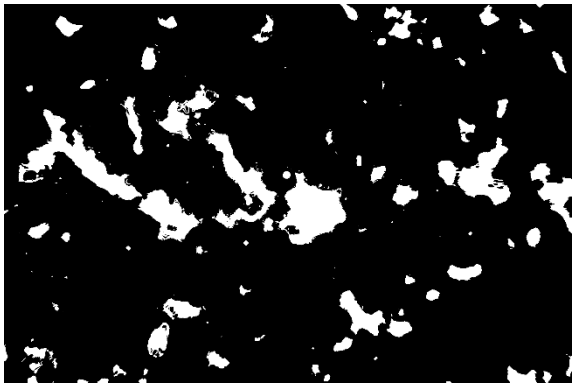

Figure 3.2: Image after thresholding in ImageJ showing porosity regions (white) (x50)

4 RESULTS

This chapter presents and analyzes the experimental results obtained during the study. The data are organized according to each specimen. Observations from stereoscopic and microscopic analysis, hardness testing, and other relevant analysis are included to support the conclusions drawn in the following chapters.

4.1 As-Built Specimens

As-Built 1:

In ***Figure 4.1***, there is a general view of the transverse section of the specimen. There are some regions, which are more interesting due to their microstructure and the specific characteristics of the method applied. Starting from the center [***Figure 4.2, Figure 4.3, Figure 4.4****]*, there are a lot of melt pools at the same direction which indicate the laser's path and confirm that this is the transverse direction of the specimen. Also, porosity is observed across the entire surface, a usual type of failure in AM processes. ***[Figure 4.5***].

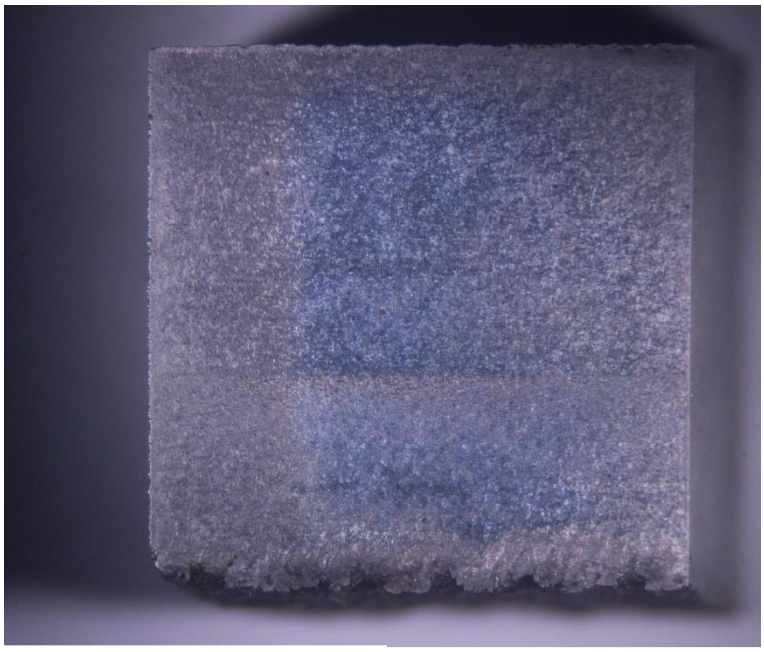

Figure 4.1: Stereoscopic transverse section of as-built 1 (x6)

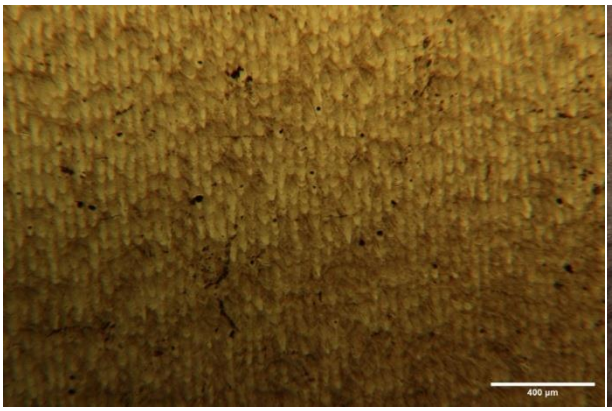

Figure 4.2: Microscopic transverse section at the center of as-built 1 (x50)

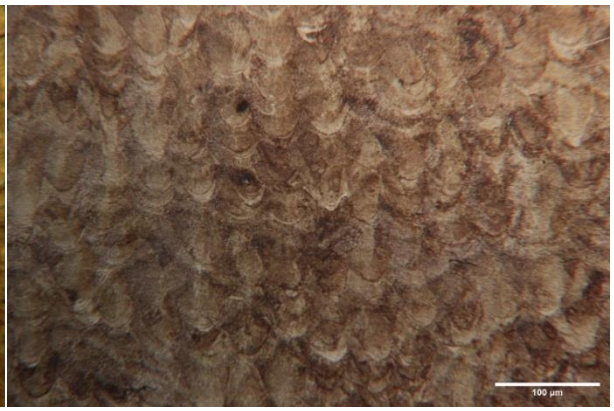

Figure 4.3: Microscopic transverse section at the center of as-built 1 (x200)

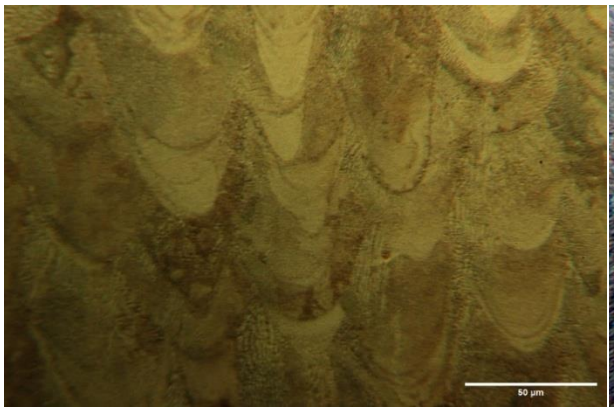

Figure 4.4: Microscopic transverse section at the center of as-built 1 (x500)

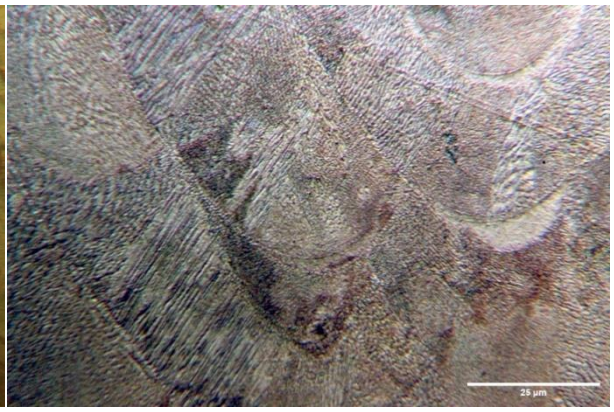

Figure 4.5: Microscopic transverse section at the center of as-built 1 (x1000)

Moreover, regarding the geometry of the melting pools in different areas, several measurements were conducted, however there is no clear average value, as significant variations are present. The calculations were carried out using ImageJ software, as it is shown in ***Figure 2.5***. More specifically, the width ranged from 20µm to 35µm and the height from 11µm to 24µm. The only region with small deviations in width and length, with average values of 31µm and 16,1µm respectively, is the center of the specimen, maybe due to homogeneity of the thermal gradients. The melt pools in different areas are shown below. [***Figure 4.6***, ***Figure 4.7***, ***Figure 4.8***, ***Figure 4.9***]

Figure 4.6: Melt pools at the top left (x500)

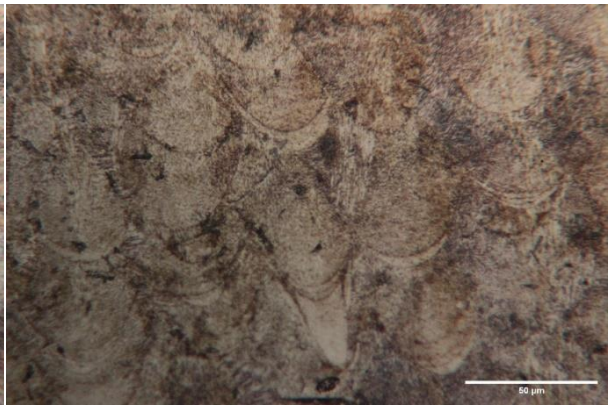

Figure 4.7: Melt pools at the top right (x500)

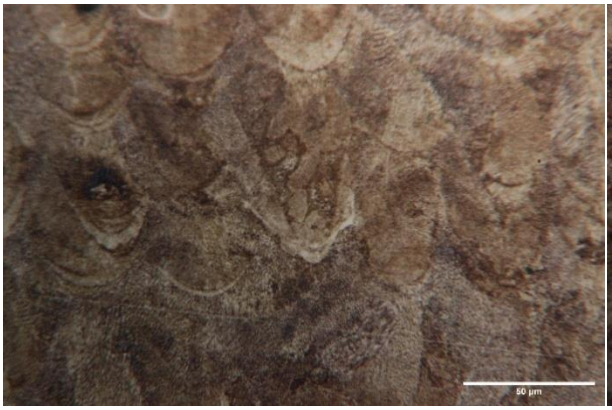

Figure 4.8: Melt pools at the center (x500)

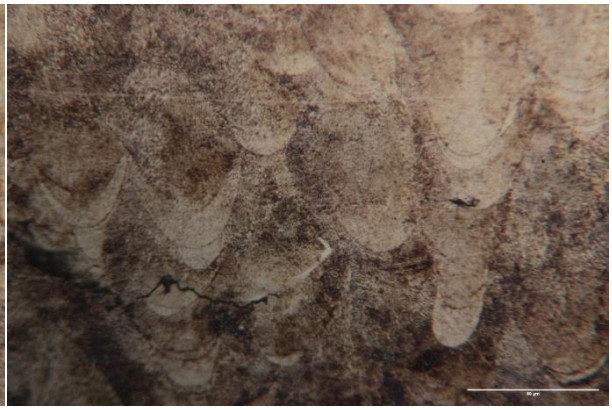

Figure 4.9: Melt pools at the bottom center (x500)

Furthermore, at some regions there are cracks, which all have the same direction. More specifically in ***Figure 4.10***, three cracks are visible at horizontal direction ***and Figure 4.11, Figure 4.12*** and ***Figure 4.13*** show magnified views of each one for better analysis.

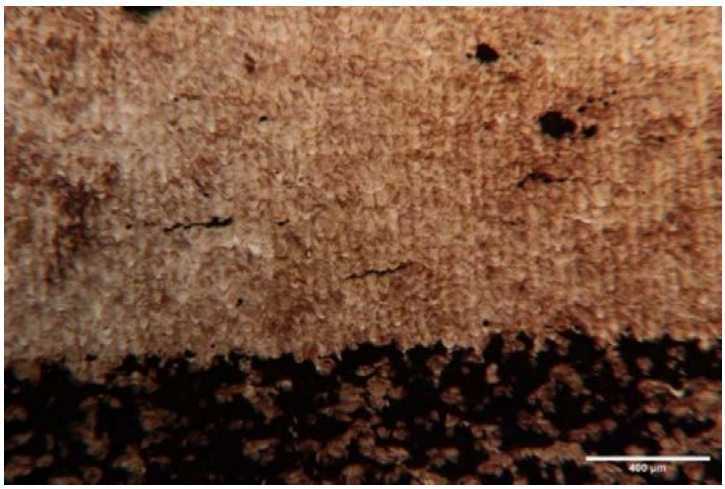

Figure 4.10: Three cracks at the center of as-built 1 (x50)

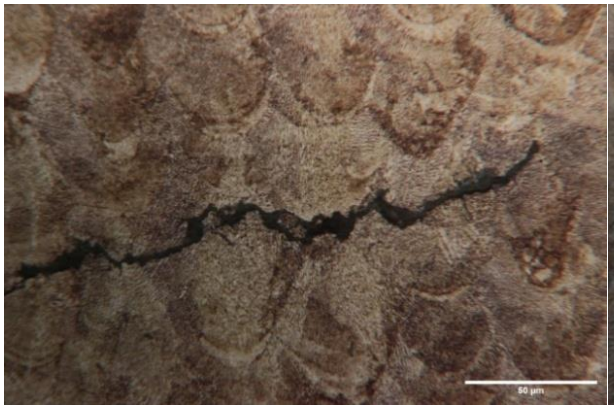

Figure 4.11:Crack 1 (x500)

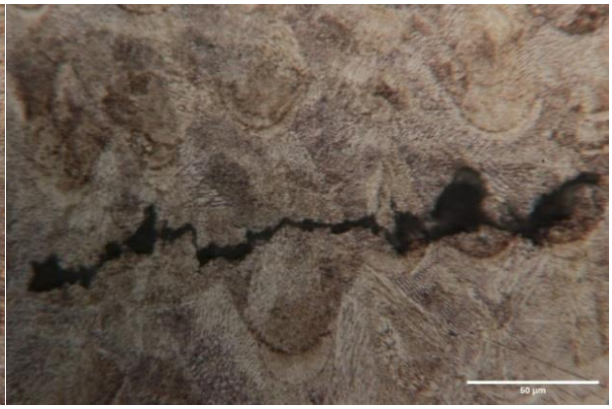

Figure 4.12: Crack 2 (x500)

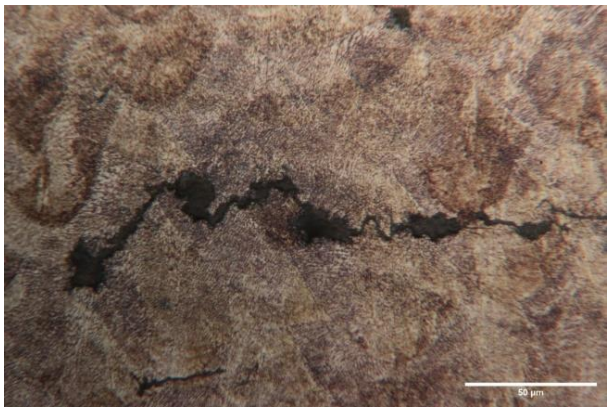

Figure 4.13: Crack 3 (x500)

Furthermore, a total of 16 hardness measurements were carried out across different areas of the specimen – 8 along the building direction and 8 along the horizontal direction, yielding an average value of 561.8 HV. It was observed that, in the building direction, hardness had an average value of 550.9 HV while in the horizontal direction a value of 572.7 HV, with small deviations. This observation agreed with the results of Lei et al. [2] who argues that hardness in the building direction is lower from the horizontal's.

In ***Figure 4.14***, there is a general view of the parallel section of the as-built 1 specimen. From closer views [***Figure 4.15, Figure 4.16, Figure 4.17, Figure 4.18***] significant porosity is clearly observed across the whole surface. It is visible that at the top right corner the porosity is higher than at the other regions of the surface.

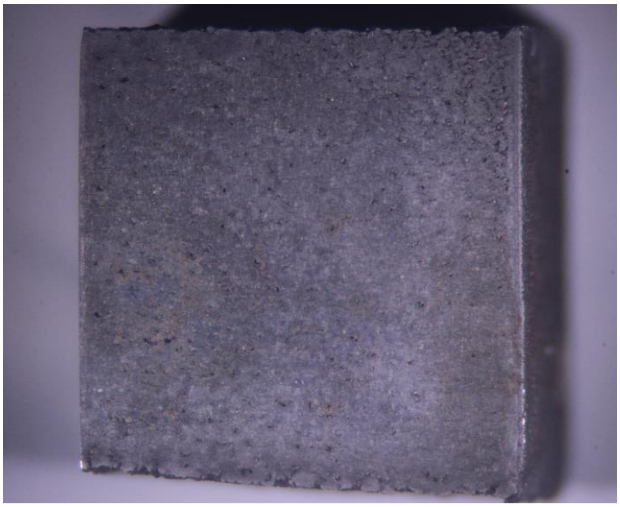

Figure 4.14: Stereoscopic parallel section of as-built 1 (x6)

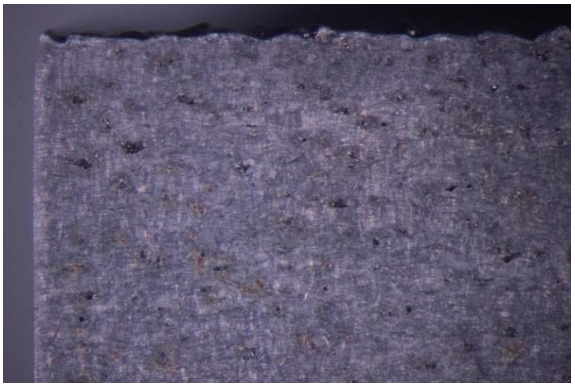

Figure 4.15: Stereoscopic parallel section at the top left corner (x13)

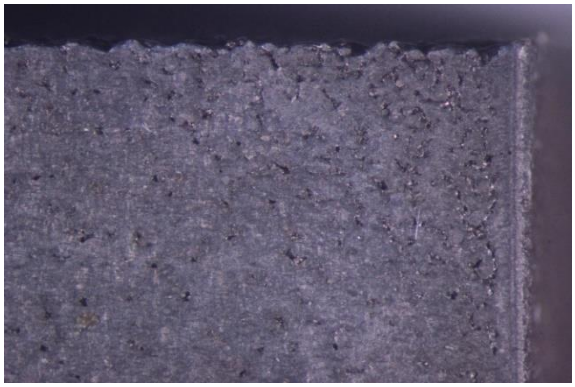

Figure 4.16: Stereoscopic parallel section at the top right corner (x13)

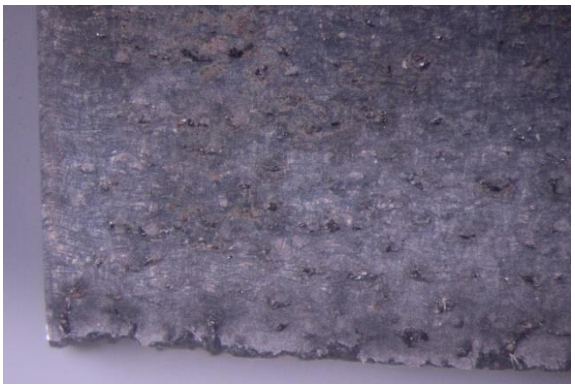

Figure 4.17: Stereoscopic parallel section at the bottom left corner (x13)

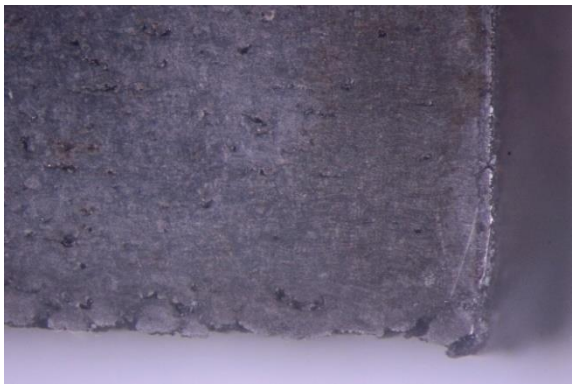

Figure 4.18: Stereoscopic parallel section at the bottom right corner (x13)

Following the stereoscopic observations, optical microscope images are presented in order to provide a more detailed examination of the microstructure on the surface of the specimen. In comparison with the transverse direction, the parallel one shows much higher porosity over its entire surface. Furthermore, the layers produced by the laser scanning paths can be distinguished in ***Figure 4.19, Figure 4.20, Figure 4.22, Figure 4.23.*** In ***Figure 4.21*** it cannot be seen clearly, due to lack of fusion. The layers appear to have a wavy form.

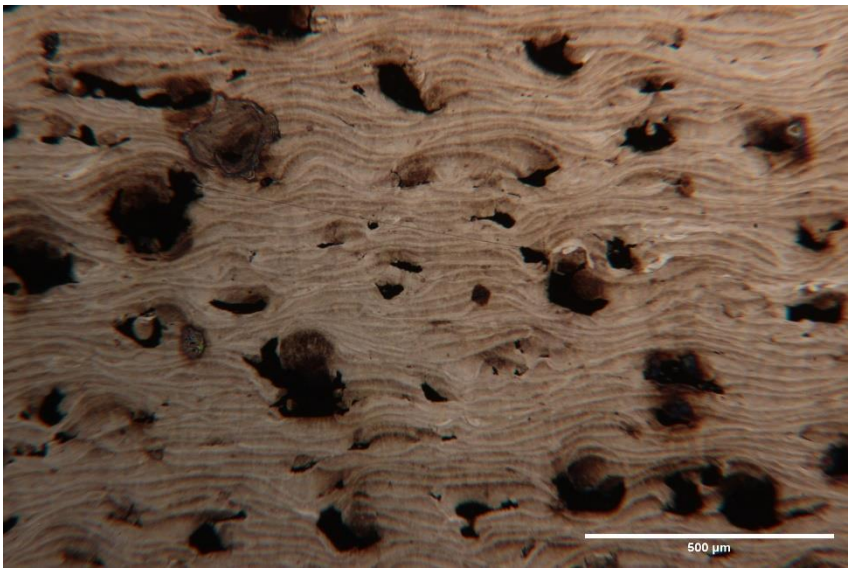

Figure 4.19: Microscopic parallel section at the center of as-built 1(x50)

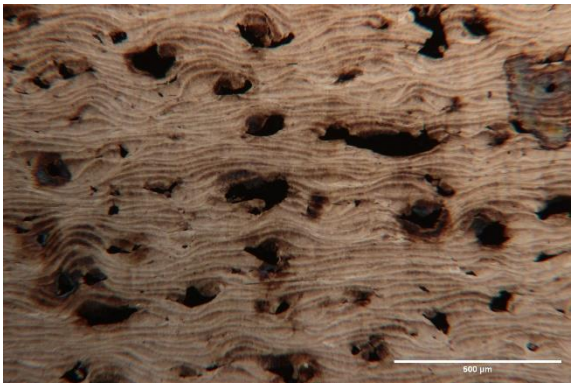

Figure 4.20: Microscopic parallel section at the top left corner of as-built 1(x50)

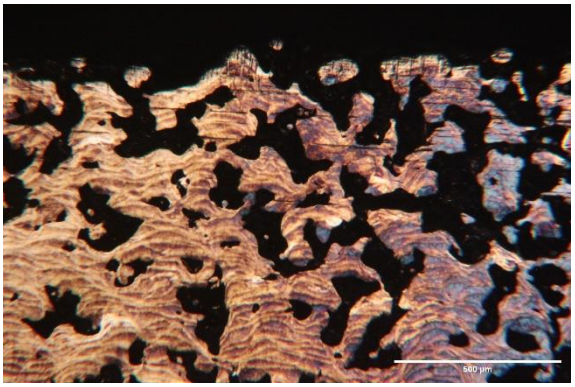

Figure 4.21: Microscopic parallel section at the top right corner of as-built 1 (x50)

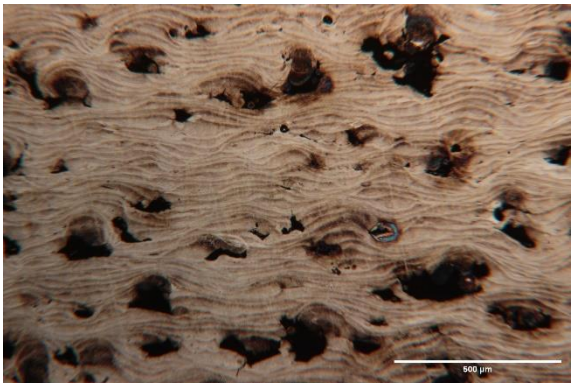

Figure 4.22: Microscopic parallel section at the bottom left corner of as-built 1(x50)

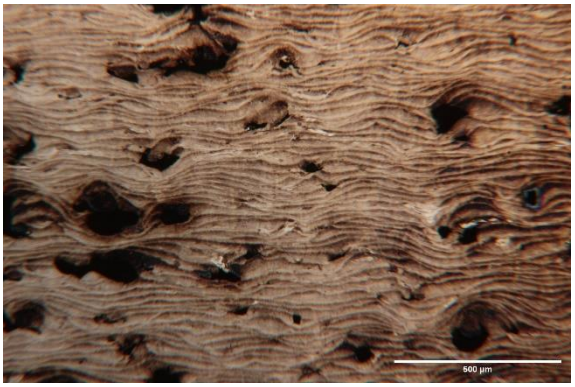

Figure 4.23: Microscopic parallel section at the bottom right corner of as-built 1(x50)

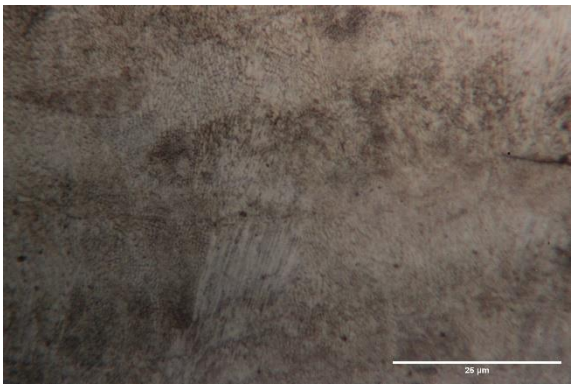

Figure 4.24: Microscopic parallel section at the top left corner of as-built 1(x1000)

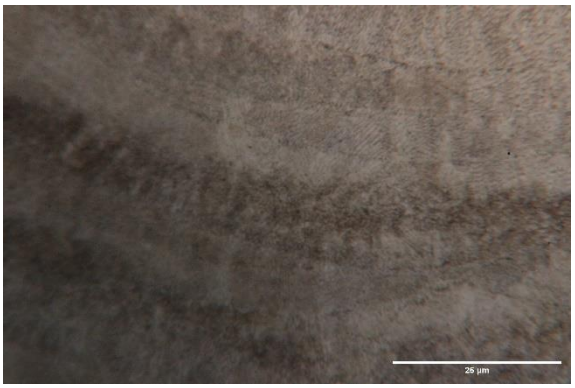

Figure 4.25: Microscopic parallel section at the center of as-built 1(x1000)

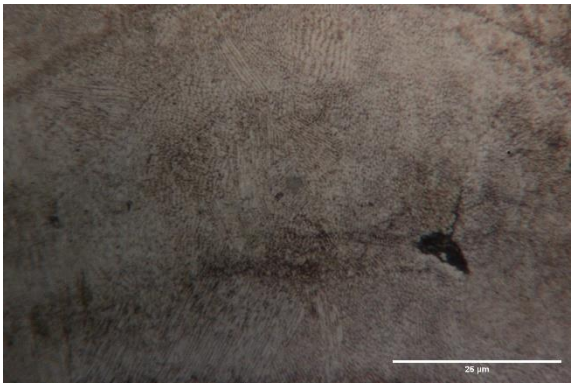

Figure 4.26: Microscopic parallel section at the bottom left corner of as-built 1(x1000)

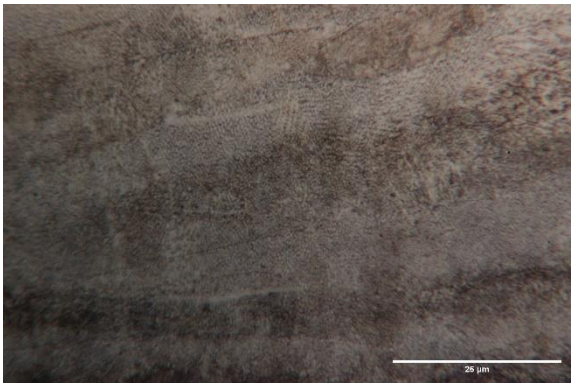

Figure 4.27: Microscopic parallel section at the bottom right corner of as-built 1 (x1000)

For the hardness tests, the same procedure as that used on the transverse side was followed, with the same number of measurements. The average value of this side was 593.95HV. More thoroughly, along the building direction, the values showed high deviations, as expected due

to the high porosity. In the horizontal direction, only small deviations were observed, with an average value of 637.9 HV. As observed, the horizontal direction exhibited higher hardness values compared to the building direction. However, a second grinding/polishing process was conducted to observe the differences in hardness. The hardness that was calculated was 555.6 HV. For this reason, a third grinding/polishing process was conducted and the hardness was 567.9HV. These high deviations in hardness are due to inhomogeneity if the SLM process.

Overall, the hardness of the as-built specimen 1, considering all the measurements taken, was found to be 567.1 HV.

As-Built 2:

The as-built 2 specimen was manufactured with different process parameters and so it's microstructure and hardness differ at some point from the others specimens. In general, as in the as -built 1, the melt pools are clearly visible on the transverse face, following a distinct orientation (***Figure 4.28***). Regarding porosity, it is also observed as a type of failure, demonstrating that is one of the most frequent challenges of the SLM method. [***Figure 4.29***, ***Figure 4.30, Figure 4.31, Figure 4.32***]

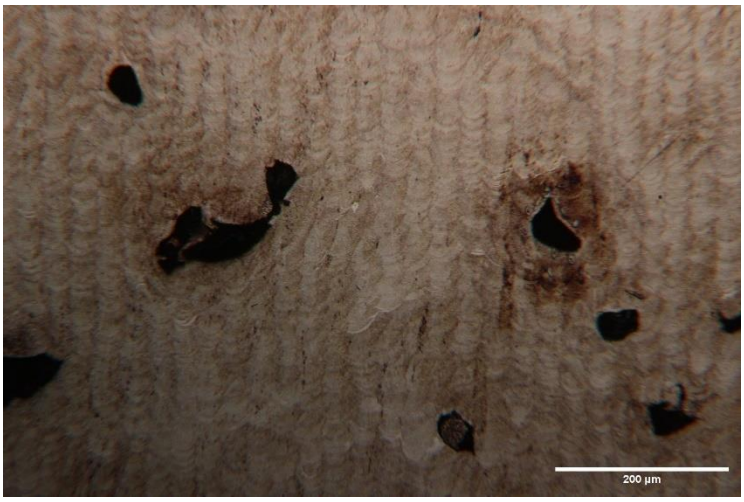

Figure 4.28: Microscopic transverse section at the center of as-built 2 (x100)

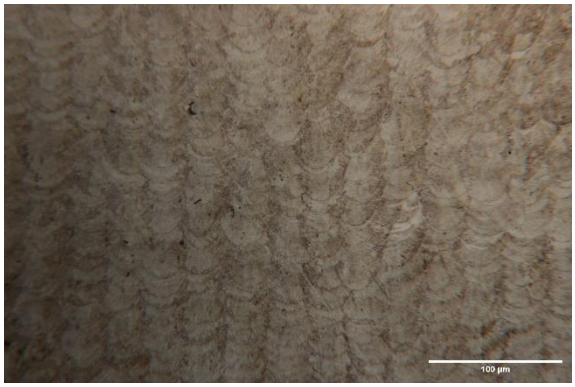

Figure 4.29: Microscopic transverse section at the top left corner of as-built 2(x200)

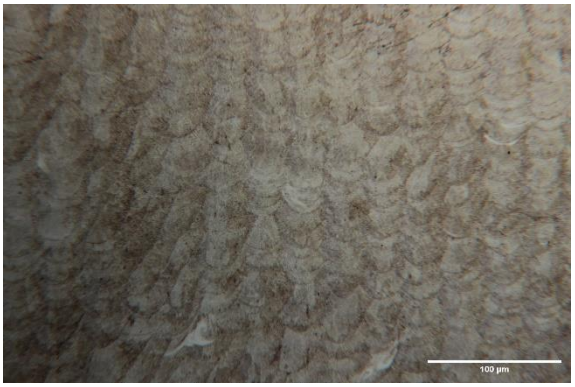

Figure 4.30: Microscopic transverse section at the top right corner of as-built 2(x200)

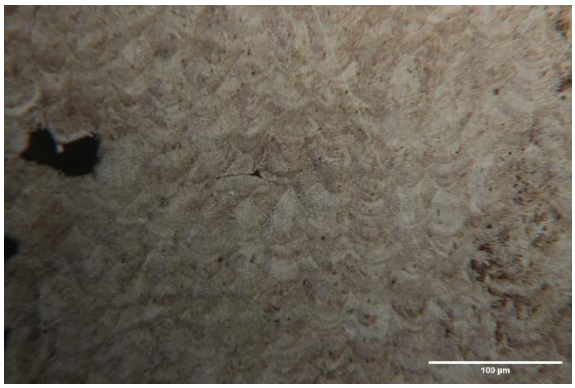

Figure 4.31: Microscopic transverse section at the bottom left corner of as-built 2(x200)

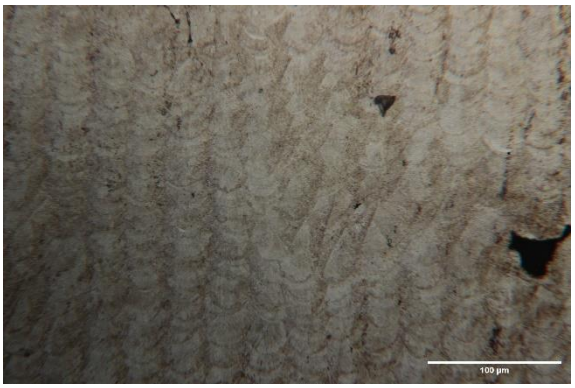

Figure 4.32: Microscopic transverse section at the bottom right corner of as-built 2(x200)

From some more magnified views, the microstructure appears to be more precise, as well as the geometry of the weld pools.

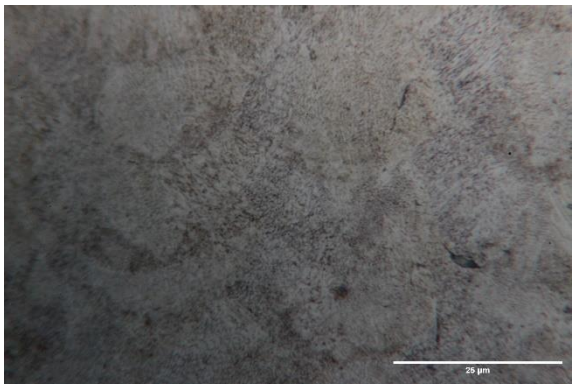

Figure 4.33: Microscopic transverse section at the top left corner of as-built 2(x1000)

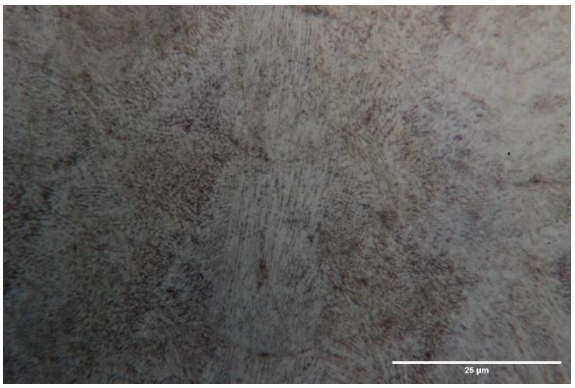

Figure 4.34: Microscopic transverse section at the top right corner of as-built 2(x1000)

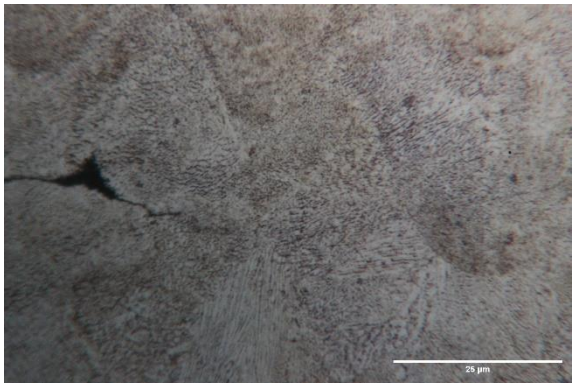

Figure 4.35: Microscopic transverse section at the bottom left corner of as-built 2(x1000)

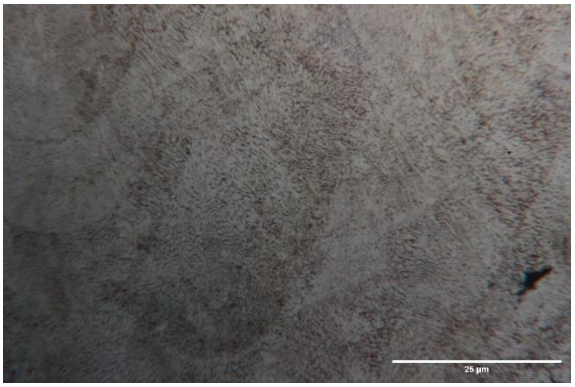

Figure 4.36: Microscopic transverse section at the bottom right corner of as-built 2(x1000)

The geometry of the weld pools was calculated and appeared to have smaller deviations compared to the geometry of the as-built 1. More specifically, the width had an average value of 26.18μm and the height had an average value of 11.74μm, considering measurements obtained over the full surface.

Moreover, hardness measurements at the transverse section of the specimen appeared to be higher than those of the as-built 1. More thoroughly, at the horizontal direction, the values showed small deviations, achieving an average value of 584.8 HV. Along the building direction, the average value was 577.4 HV. The average hardness value across the entire transverse section was 581.1 HV.

In ***Figure 4.37***, there is a general view of the parallel section of the as-built 2 specimen. From closer views [***Figure 4.38, Figure 4.39, Figure 4.40, Figure 4.41***] significant porosity is clearly observed across the whole surface. It is visible that at the top and bottom right corners the porosity is higher than at the other regions of the surface.

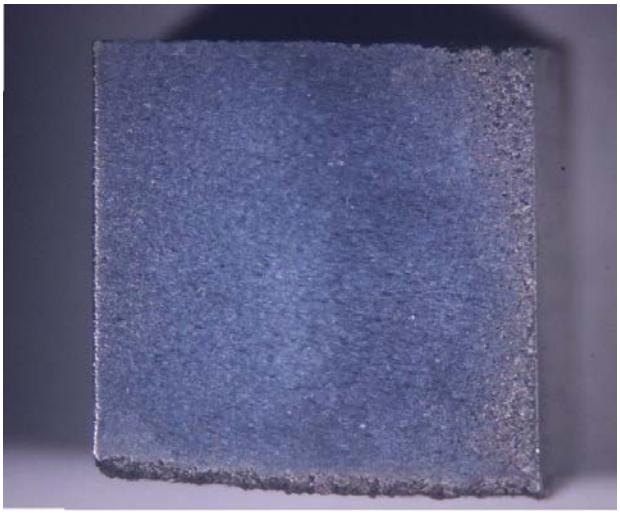

Figure 4.37: Stereoscopic parallel section of as-built 2 (x6)

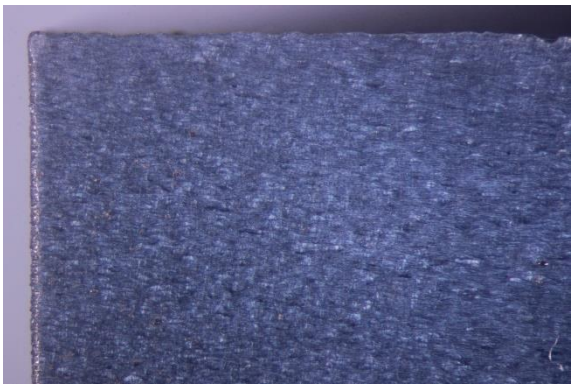

Figure 4.38: Stereoscopic parallel section at the top left corner (x16)

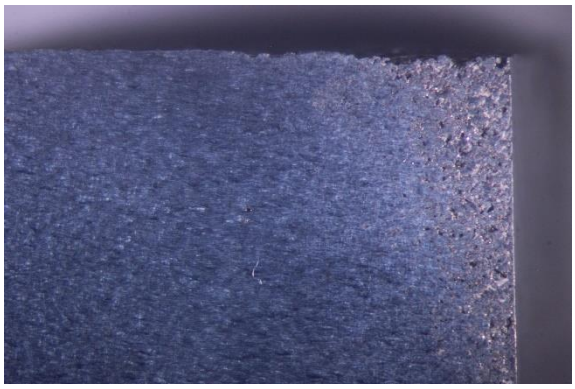

Figure 4.39: Stereoscopic parallel section at the top right corner (x16)

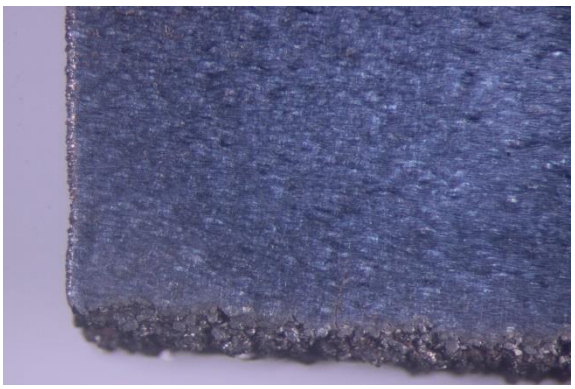

Figure 4.40: Stereoscopic parallel section at the bottom left corner (x16)

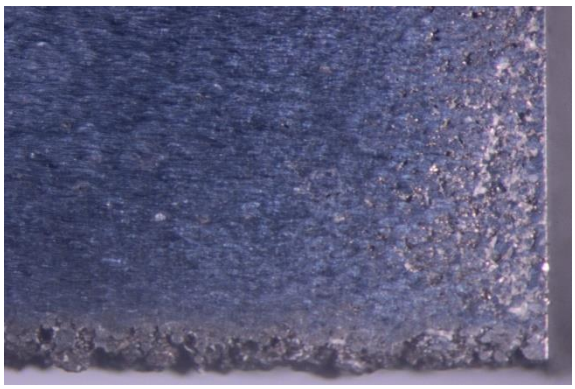

Figure 4.41: Stereoscopic parallel section at the bottom right corner (x16)

Following the stereoscopic observations, optical microscope images are presented in order to provide a more detailed examination of the microstructure on the surface of the specimen. In comparison with the transverse direction, the parallel one shows much higher porosity over

its entire surface. Furthermore, the layers produced by the laser scanning paths can be distinguished in ***Figure 4.42, Figure 4.43, Figure 4.44, Figure 4.45, Figure 4.46***. The layers appear again to have a wavy form.

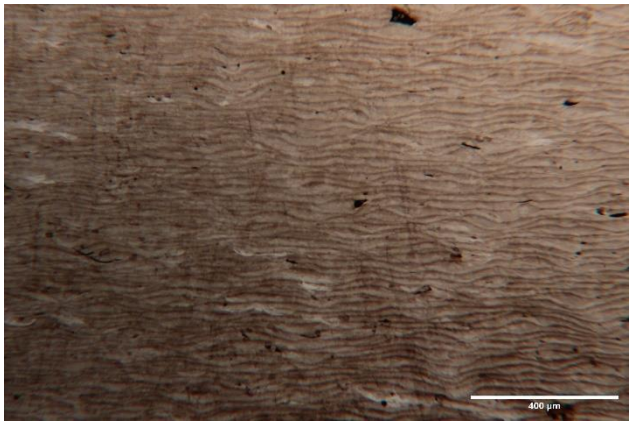

Figure 4.42: Microscopic parallel section at the center of as-built 2(x50).

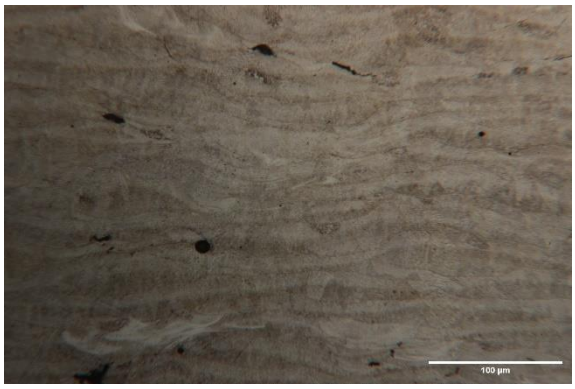

Figure 4.43: Microscopic parallel section at the top left corner of as-built 2 (x200)

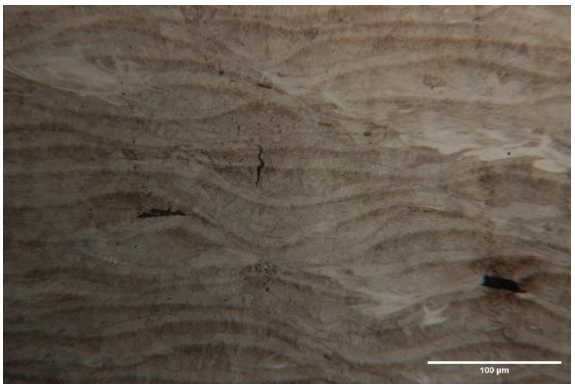

Figure 4.44: Microscopic parallel section at the top right corner of as-built 2 (x200)

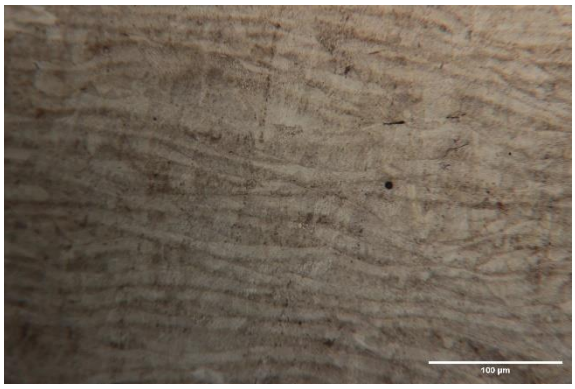

Figure 4.45: Microscopic parallel section at the bottom left corner of as-built 2 (x200)

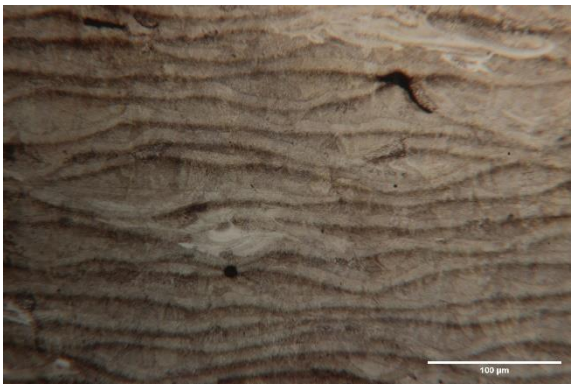

Figure 4.46: Microscopic parallel section at the bottom right corner of as-built 2 (x200)

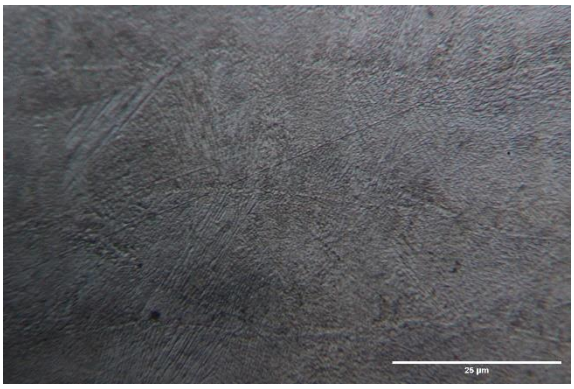

Figure 4.47: Microscopic parallel section at the top left corner of as-built 2(x1000)

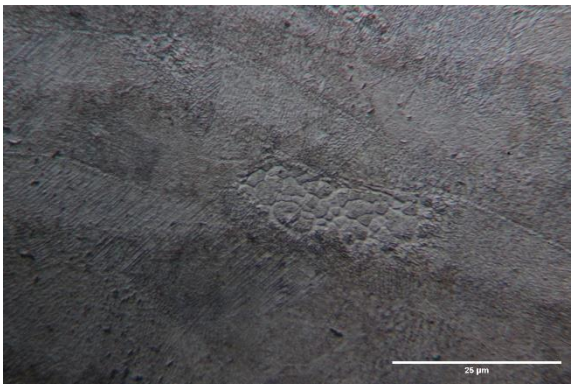

Figure 4.48: Microscopic parallel section at the center of as-built 2(x1000)

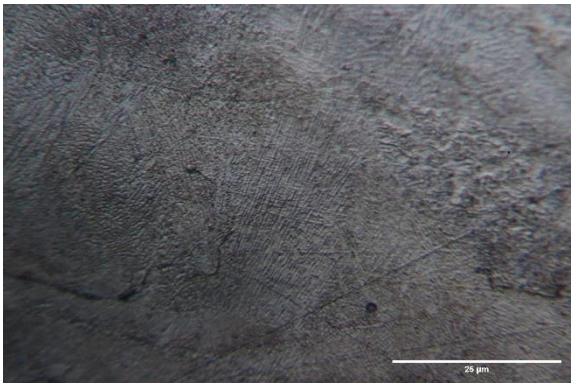

Figure 4.49: Microscopic parallel section at the top left corner of as-built 2(x1000)

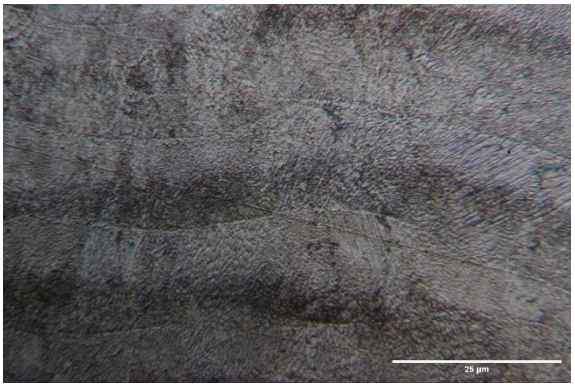

Figure 4.50: Microscopic parallel section at the bottom right corner of as-built 2(x1000)

The microscopic analysis of this specimen proved that cracking is also a common defect of this method. ***Figure 4.51*** and ***Figure 4.52*** present cracks originating from the side edge, probably because of porosity on the surface, which might propagate to the inside of the sample.

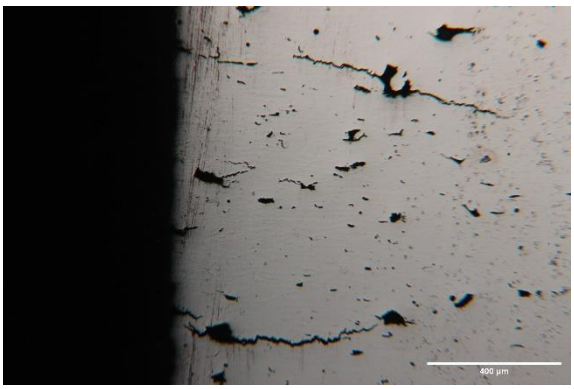

Figure 4.51: Crack originating from the top left edge of the as-built 2 (×50).

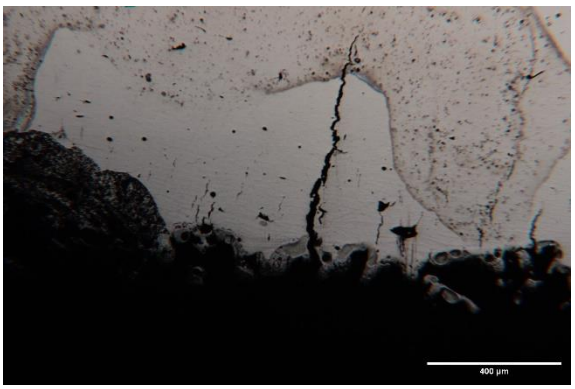

Figure 4.52: Crack propagating from the bottom center edge of the as-built 2 (×50).

Figure 4.53 and ***Figure 4.54*** present some microcracks found on the inside of the sample, maybe due to residual stresses between the layers.

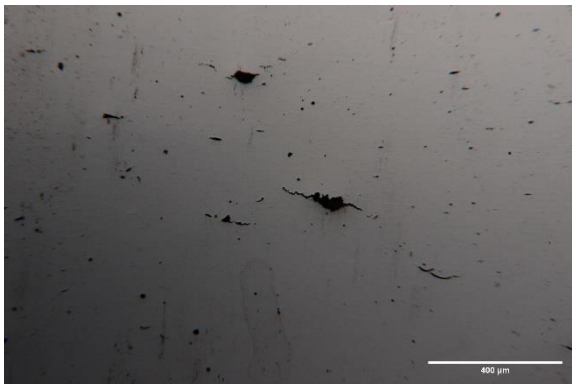

Figure 4.53: Microcracks observed in the top left corner of the as-built 2 (×50).

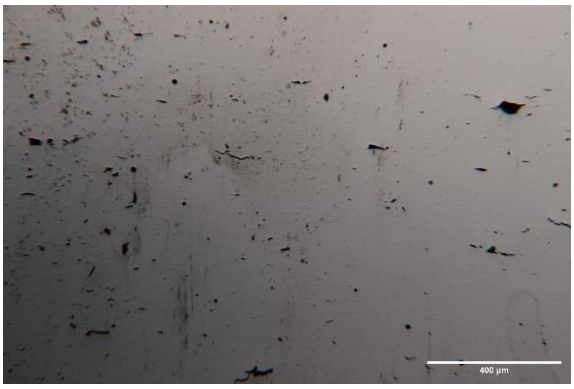

Figure 4.54: Microcracks in the bottom left corner of the as-built 2 (×50).

The hardness measurements on the parallel side showed that the hardness is slightly lower compared to the transverse side, with an average value of 553.9 HV.

Overall, the hardness of the as-built specimen 2, considering all the measurements taken, was found to be 567.5 HV.

As-Built 3:

In ***Figure 4.55*** there is a general stereoscopic view of the transverse side as-built 3 specimen, while in ***Figure 4.56*** there is a general view of the parallel one.

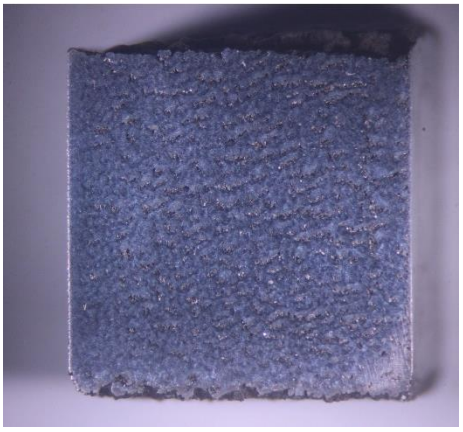

Figure 4.55: Stereoscopic transverse section of as-built 3 (x6)

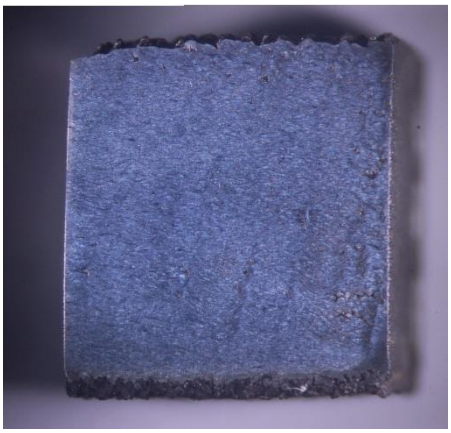

Figure 4.56: Stereoscopic parallel section of as-built 3 (x6)

The main defect that was observed in the transverse side of this specimen was a high amount of lack of fusion pores across the entire surface (Figure 4.57). In there are microscopic pictures from every part of the transverse section, depicting the high percentage of LoF. Moreover, there are some unmelted powder particles inside the LoF pores. Although melt pools must be visible theoretically, in this side they are not so clear due to porosity.

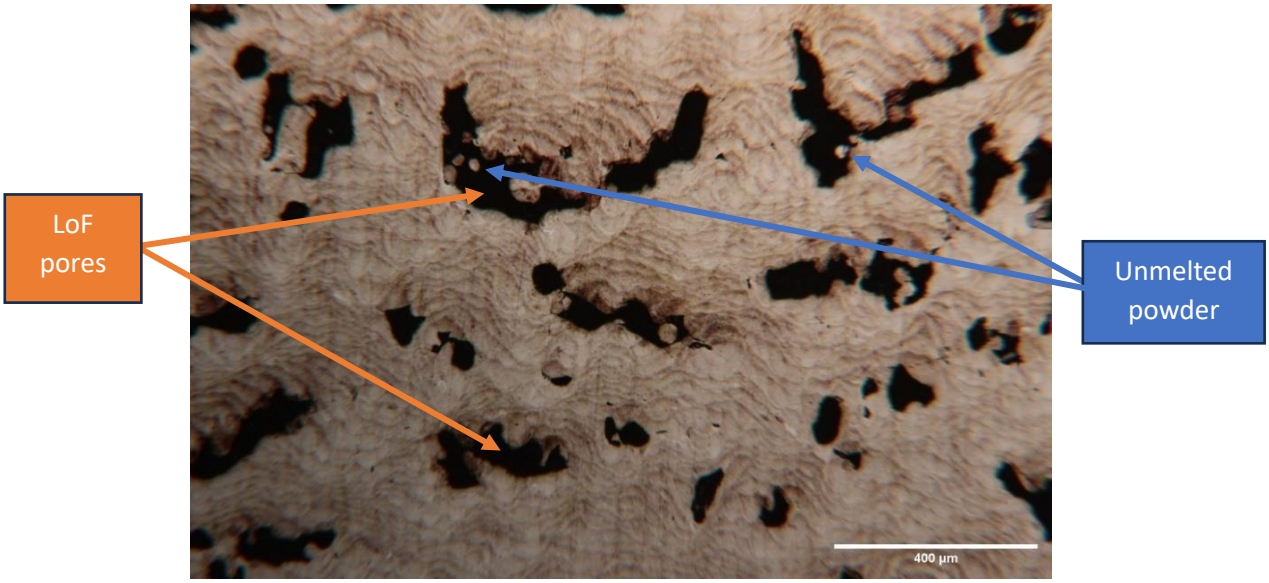

Figure 4.57: Lack of fusion pores with unmelted powder in the transverse section at the center of as-built 3(x50).

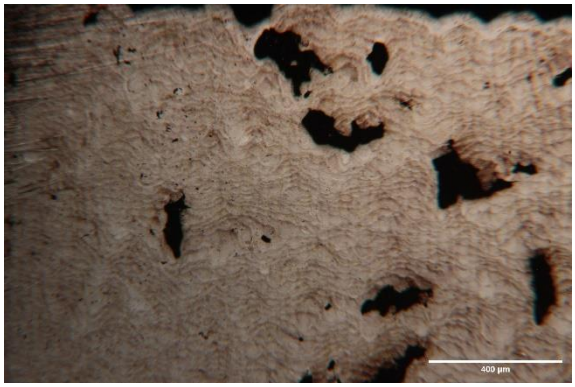

Figure 4.58: Microscopic transverse section at the top left corner of as-built 3 (x50)

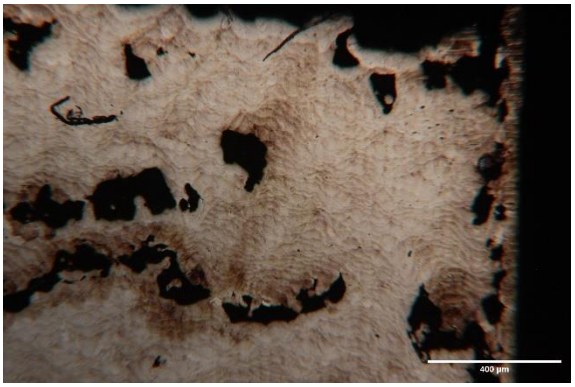

Figure 4.59: Microscopic transverse section at the top right corner of as-built 3 (x50)

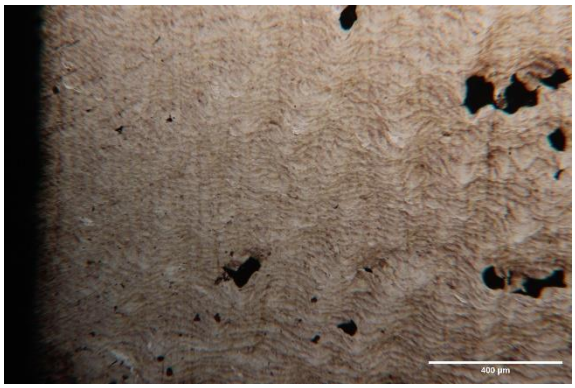

Figure 4.60: Microscopic transverse section at the bottom left corner of as-built 3 (x50)

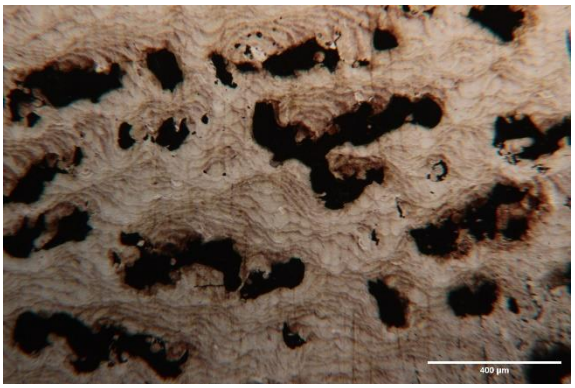

Figure 4.61: Microscopic transverse section at the bottom right corner of as-built 3 (x50)

Regarding the microstructure, in ***Figure 4.62***, ***Figure 4.63***, ***Figure 4.64***, ***Figure 4.65***, ***Figure 4.66*** there are magnified views from the entire surface of the transverse section, at the parts that there is no lack of fusion.

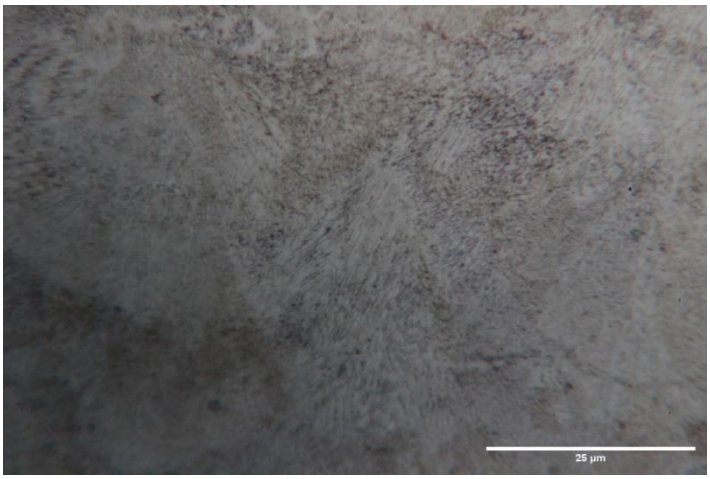

Figure 4.62: Microscopic transverse section at the center of as-built 3 (x1000)

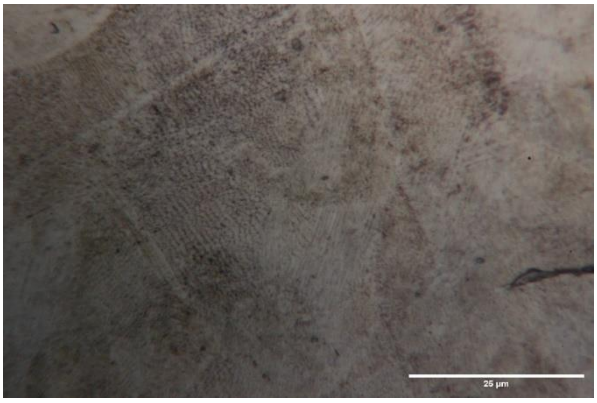

Figure 4.63: Microscopic transverse section at the top left corner of as-built 3 (x1000)

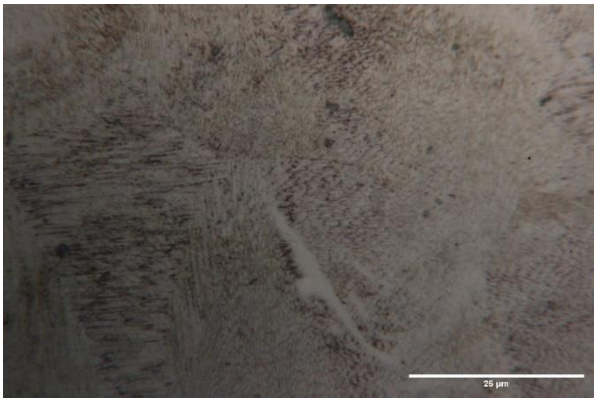

Figure 4.64: Microscopic transverse section at the top right corner of as-built 3 (x1000)

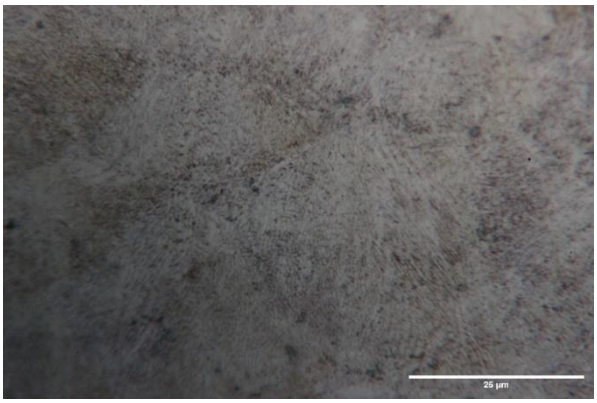

Figure 4.65: Microscopic transverse section at the top left corner of as-built 3 (x1000)

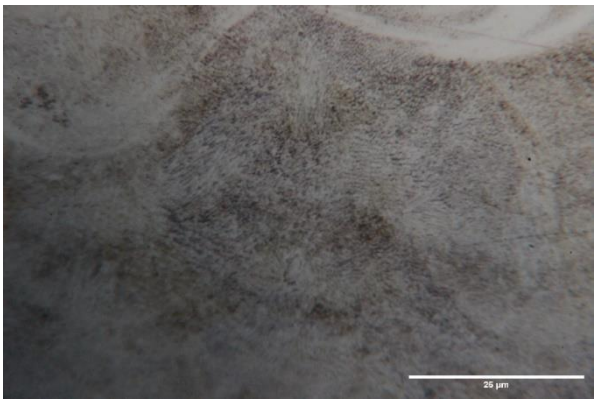

Figure 4.66: Microscopic transverse section at the top right corner of as-built 3 (x1000)

The geometry of the weld pools of the as-built 3 was not easy to be calculated properly, maybe because of high laser power and more wavy form of the microstructure (***Figure 4.57***).

Moreover, hardness measurements at the transverse section of the as-built 3 specimen appeared to be lower than those of the as-built 2. More thoroughly, at the horizontal direction, the values showed small deviations, achieving an average value of 573.8 HV. Along the building direction, the average value was 563.8HV. The average hardness value across the entire transverse section was 568.8HV.

As for the parallel side of as-built 3, there was slightly lower porosity compared to the transverse side [Figure 4.67, ***Figure 4.68***, ***Figure 4.70***]. However, the right side of the specimen suffered a lot from lack of fusion porosity [***Figure 4.69***, ***Figure 4.71***].

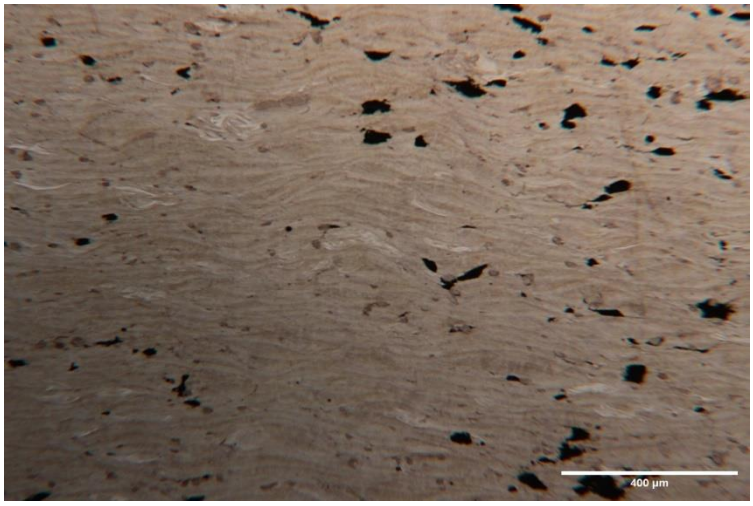

Figure 4.67: Lack of fusion pores in the parallel section at the center of as-built 3(x50)

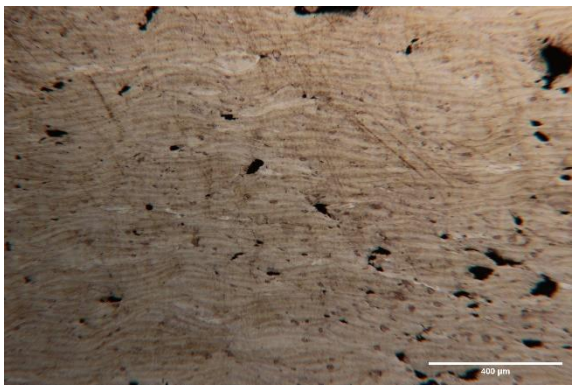

Figure 4.68: Microscopic parallel section at the top left corner of as-built 3 (x50)

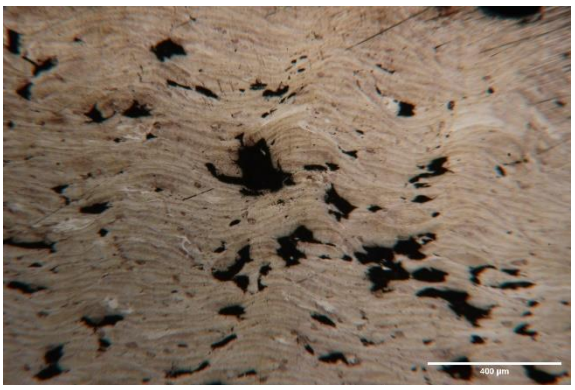

Figure 4.69: Microscopic parallel section at the top right corner of as-built 3 (x50)

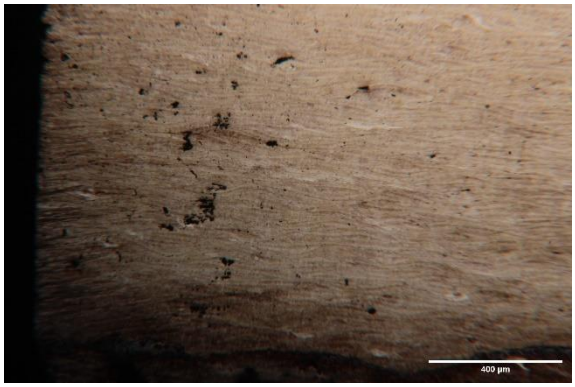

Figure 4.70: Microscopic parallel section at the bottom left corner of as-built 3 (x50)

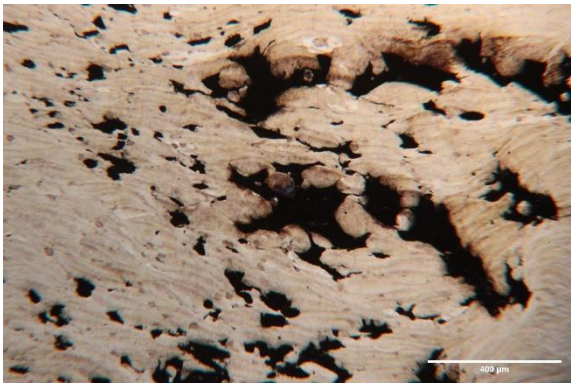

Figure 4.71: Microscopic parallel section at the bottom right corner of as-built 3 (x50)

The hardness measurements on the parallel side showed that the hardness is lower compared to the transverse side, with an average value of 555.3 HV.

Overall, the hardness of the as-built specimen 3, considering all the measurements taken, was found to be 562 HV.

The following ***Table 4.1*** summarizes the hardness measurements of the as-built specimens.

Table 4.1 Hardness measurements of the as-built specimens.

Hardness (HV)	**As-built 1**	**As-Built 2**	**As-Built 3**
Transverse side	563	581.1	568.8
Parallel side	571.2	553.9	555.3
Mean	567.1	567.5	562.0

Moreover, porosity calculations of the as-built specimens were carried out using ImageJ software. The following ***Table 4.2*** summarizes the porosity calculations of the as-built specimens.

Table 4.2 Porosity measurements of the as-built specimens.

Porosity (%)	**As-Built 1**	**As-Built 2**	**As-Built 3**
Transverse side	2.94	5.56	10.32
Parallel side	4.83	7.89	4.74
Mean	3.89	6.72	7.53

4.2 Heat-Treated Specimens

The heat-treated specimens were those that after they were manufactured with SLM, they were quenched in ambient air and then tempered twice at 580^{o}C for 2 hours. The difference in the microstructure compared to the as-built specimens is that the weld pools and the layering at each side are not visible in the heat-treated specimens, probably due to austenitizing. As a result, there are no obvious differences on each side.

Heat-treated 1:

In Figure 4.72, Figure 4.73, ***Figure 4.74***, ***Figure 4.75***, ***Figure 4.76***, ***Figure 4.77***, magnified views of the transverse side of the heat-treated 1 specimen are presented. A non-uniform distribution of the microstructure can be observed at the same magnification (***Figure 4.73***, ***Figure 4.74***, ***Figure 4.75***, ***Figure 4.76***, ***Figure 4.77***), which can be attributed to the inherent non-uniformity of the SLM process.

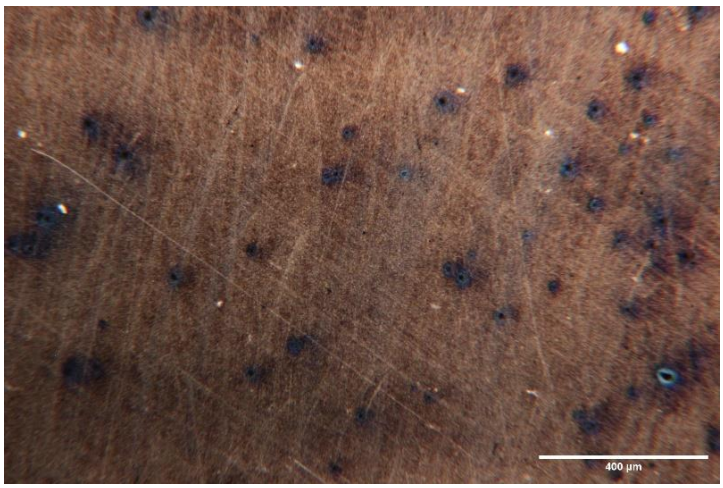

Figure 4.72: Microscopic transverse section at the center of heat-treated 1 (x50)

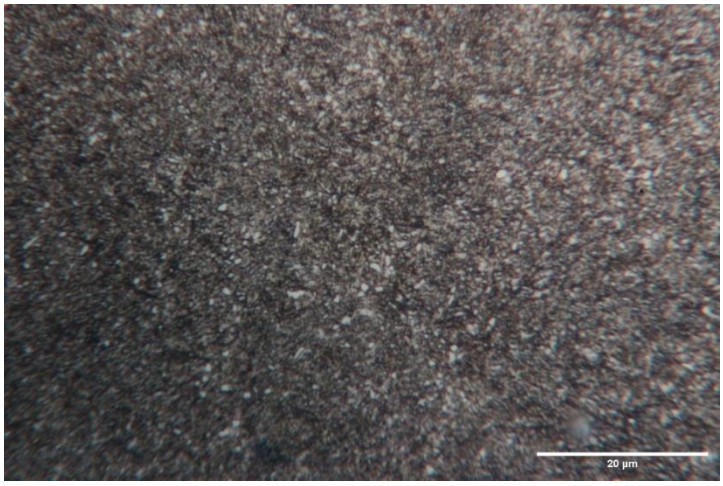

Figure 4.73: Microscopic transverse section at the center of heat-treated 1 (x1000)

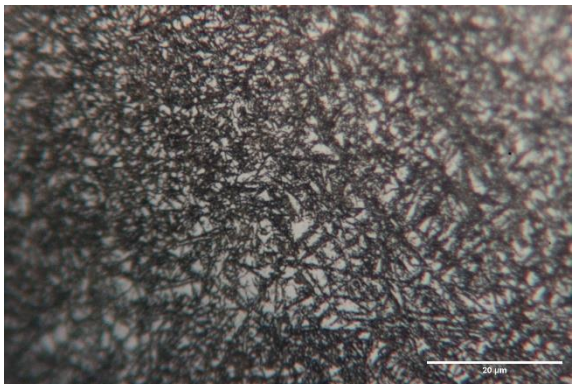

Figure 4.74: Microscopic transverse section at the top left corner of heat-treated 1 (x1000)

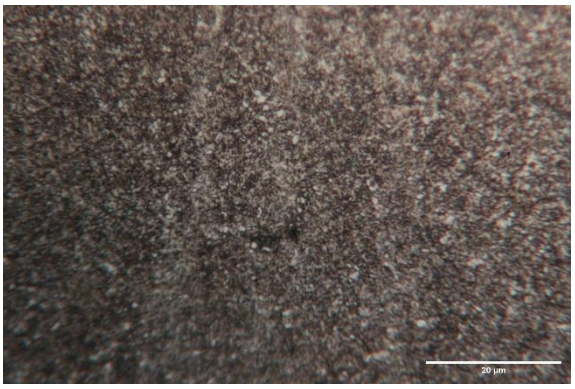

Figure 4.75: Microscopic transverse section at the top right corner of heat-treated 1 (x1000)

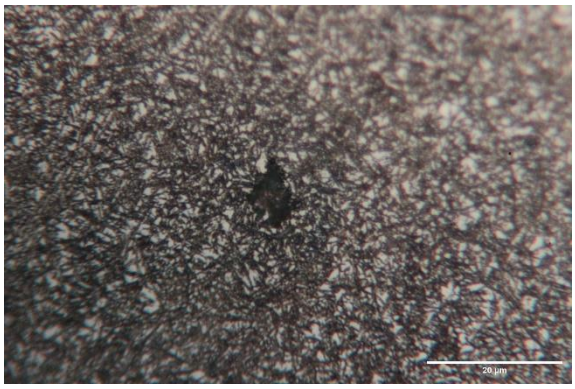

Figure 4.76: Microscopic transverse section at the bottom left corner of heat-treated 1 (x1000)

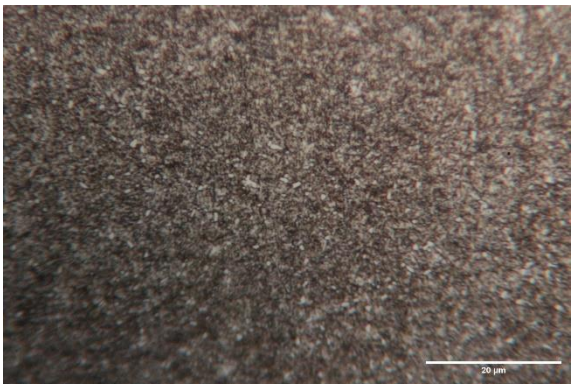

Figure 4.77: Microscopic transverse section at the bottom right corner of heat-treated 1 (x1000)

The following images correspond to the parallel side. [***Figure 4.78***, ***Figure 4.79***, ***Figure 4.80***, ***Figure 4.81***] A similar microstructure, as discussed above for the transverse side, is observed also here:

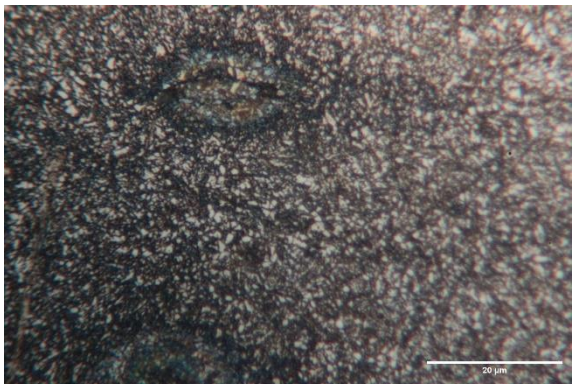

Figure 4.78: Microscopic parallel section at the top left corner of heat-treated 1 (x1000)

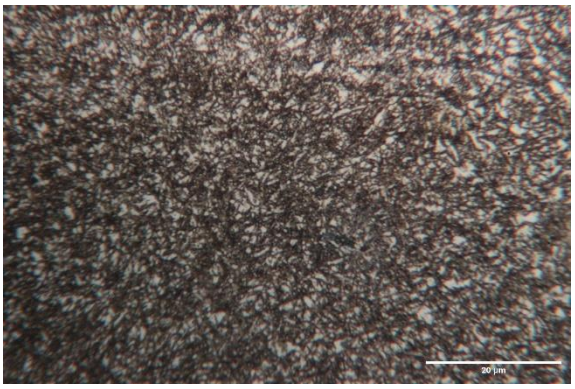

Figure 4.79: Microscopic parallel section at the center of heat-treated 1 (x1000)

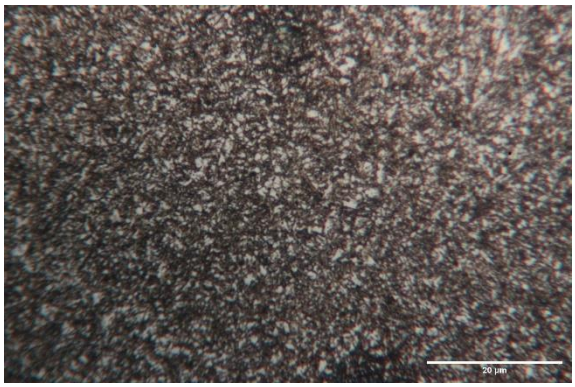

Figure 4.80: Microscopic parallel section at the bottom left corner of heat-treated 1 (x1000)

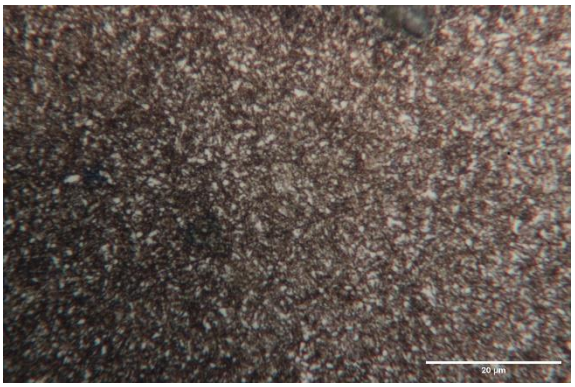

Figure 4.81: Microscopic parallel section at the bottom right corner of heat-treated 1 (x1000)

Heat-treated 2:

In ***Figure 4.82***, ***Figure 4.83***, ***Figure 4.84***, magnified views of the transverse side of the heat-treated 2 specimen are presented:

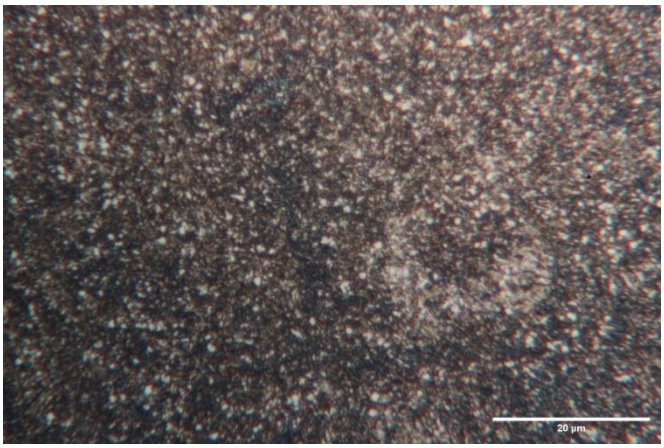

Figure 4.82: Microscopic transverse section at the center of heat-treated 2 (x1000)

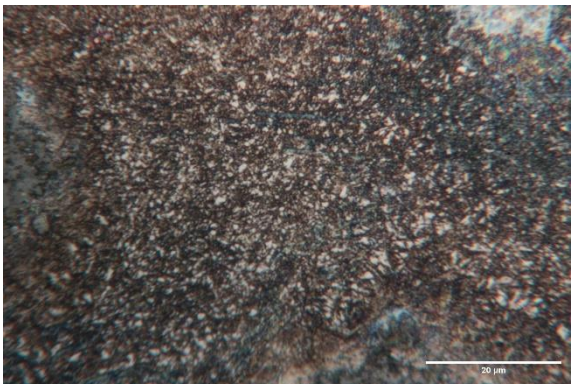

Figure 4.83: Microscopic transverse section at the top left corner of heat-treated 2 (x1000)

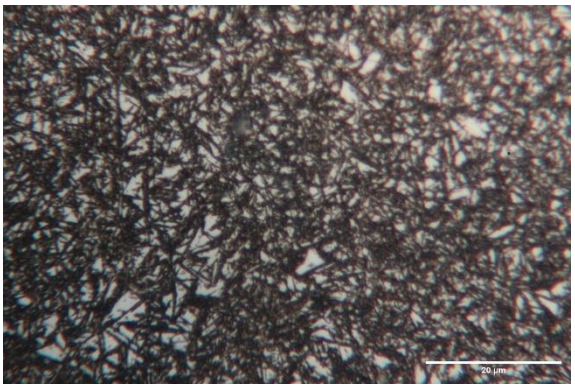

Figure 4.84: Microscopic transverse section at the bottom left corner of heat-treated 2 (x1000)

The following images correspond to the parallel side. Two large white regions can be observed in ***Figure 4.85*** and ***Figure 4.87***, however their precise identification was not possible, because chemical analysis could not be performed. [***Figure 4.85***, ***Figure 4.86***, ***Figure 4.87***, ***Figure 4.88***]

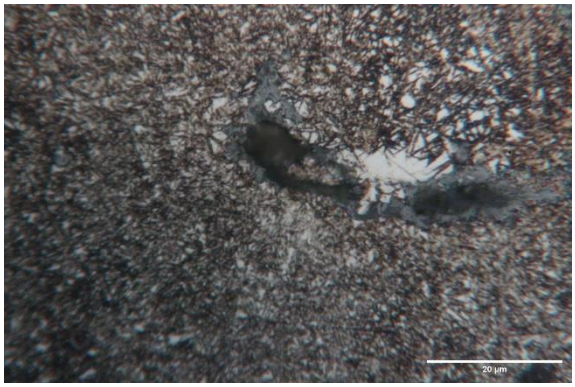

Figure 4.85: Microscopic parallel section at the center of heat-treated 2 (x1000)

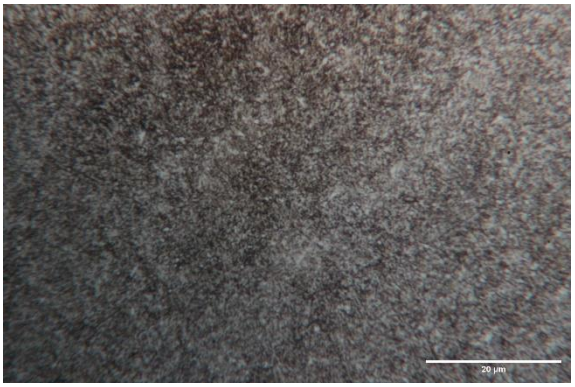

Figure 4.86: Microscopic parallel section at the center of heat-treated 2 (x1000)

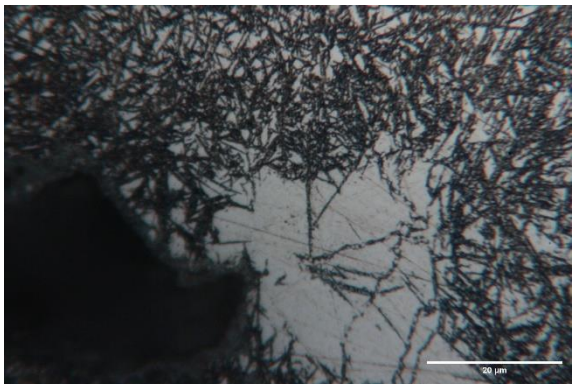

Figure 4.87: Microscopic parallel section at the bottom right corner of heat-treated 2 (x1000)

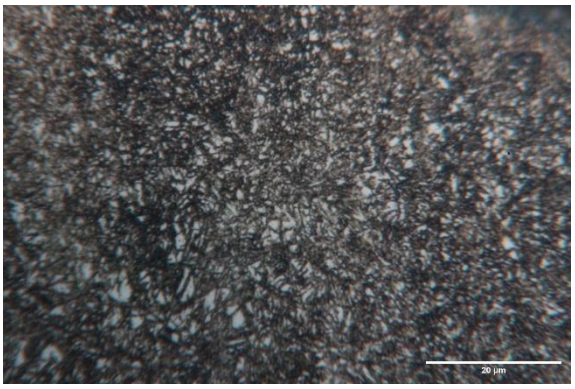

Figure 4.88: Microscopic parallel section at the bottom right corner of heat-treated 2 (x1000)

Heat-treated 3:

In ***Figure 4.89, Figure 4.90, Figure 4.91***, magnified views of the transverse side of the heat-treated 2 specimen are presented:

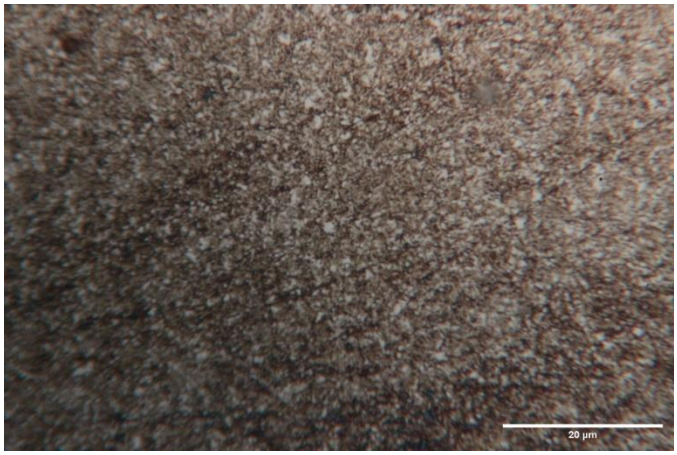

Figure 4.89: Microscopic transverse section at the center of heat-treated 3 (x1000)

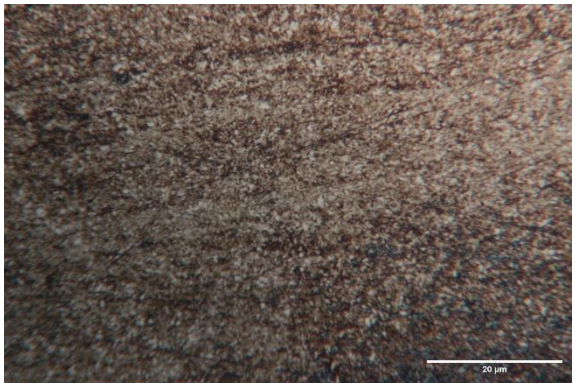

Figure 4.90: Microscopic transverse section at the bottom center of heat-treated 3 (x1000)

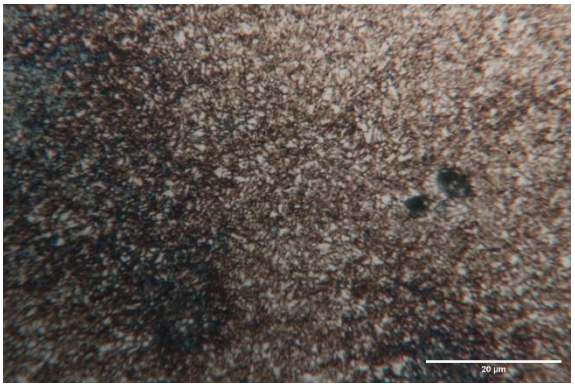

Figure 4.91: Microscopic transverse section at the top right corner of heat-treated 3 (x1000)

The following images correspond to the parallel side. [***Figure 4.92***, ***Figure 4.93***, ***Figure 4.94***, ***Figure 4.95***]

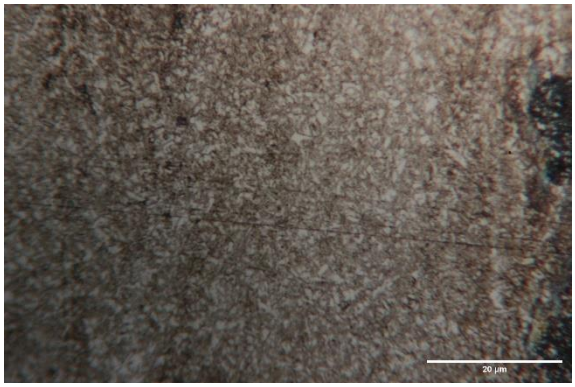

Figure 4.92: Microscopic parallel section at the top left corner of the heat-treated 3 (x1000)

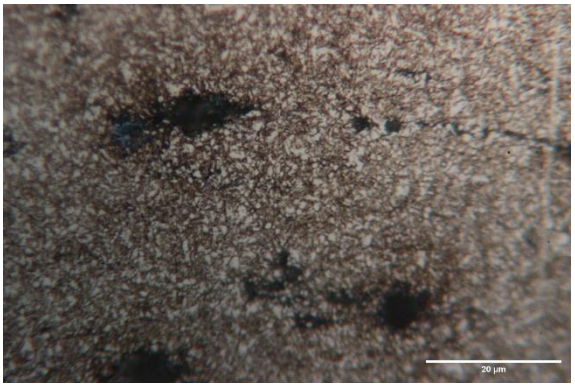

Figure 4.93: Microscopic parallel section at the bottom right corner of the heat-treated 3 (x1000)

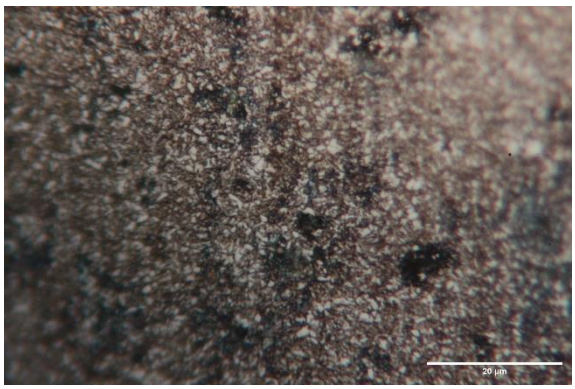

Figure 4.94: Microscopic parallel section at the bottom left corner of heat-treated 3 (x1000)

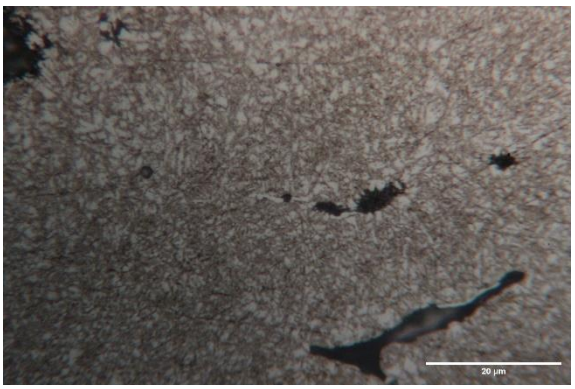

Figure 4.95: Microscopic parallel section at the bottom center of the heat-treated 3 (x1000)

The main reason of tempering the specimens was to increase their hardness. Hardness measurements were carried out from the heat-treated specimens and the results are presented in ***Table 4.4.***

Table 4.3 Hardness measurements of the heat-treated specimens.

Hardness (HV)	**Heat-Treated 1**	**Heat-Treated 2**	**Heat-Treated 3**
Transverse side	576.5	596.6	599.3
Parallel side	621.2	503.6	600.9
Mean	598.8	550.1	600.1

Porosity measurements were carried out from the heat-treated specimens and the results are presented in ***Table 4.4.***

Table 4.4 Porosity measurements of the heat-treated specimens.

Porosity (%)	**Heat-Treated 1**	**Heat-Treated 2**	**Heat-Treated 3**
Transverse side	1.75	8.49	1.88
Parallel side	10.04	10.89	6.77
Mean	5.89	9.69	4.32

Table 1.1 provides a summary of all the findings regarding porosity and hardness obtained in this study.

Table 4.5 Summarized measurements of all the six specimens.

Specimen	**Transverse Hardness (HV)**	**Parallel Hardness (HV)**	**Mean Hardness (HV)**	**Density (%)**
As-Built 1	563	571.2	567.1	96.1
As-Built 2	581.1	553.9	567.5	93.3
As-Built 3	568.8	555.3	562	92.5
Heat-Treated 1	576.5	621.2	598.8	94.1
Heat-Treated 2	596.6	503.6	550.1	90.3
Heat-Treated 3	599.3	600.9	600.1	95.7

5 CONCLUSIONS

The objective of the present thesis was to achieve an insight in the effect of process parameters and post tempering treatment on the microstructural evolution of H13 tool steel in additive manufacturing. Summarizing, the following remarks can be made:

- There are some metallurgical defects in as-fabricated H13 tool steel samples by SLM, such as pores in different sizes, lack of fusion (LoF) and cracking.
- The most common defect that the specimens of this study suffered was lack of fusion pores. This is probably due to high scanning speeds, a parameter that is inversely proportional to porosity.
- Cracking was also a common defect that was observed. Most of the cracks produced in H13 samples originate from the side edge of the sample, they propagate along the formed layer to the inside of the sample and finally terminate at the inside of the sample. There were also cracks inside the specimens, which were probably produced due to local stress concentration.
- Hardness increases relative to decreasing porosity in the as-built as well as for the heat-treated specimens.
- From the six specimens that were analyzed, the optimum choice is the heat-treated 3 specimen, as it exhibited the highest hardness (600.1HV) and density values (95.7%). The optimum process parameters found in this study was VED=135J/mm^3, P=135W, v=1000mm/s, hatch space=40μm and layer thickness t=25μm.
- The microstructure of both the as-built and the heat-treated specimens is as expected according to the literature. More specifically, the as-built microstructure consists predominantly of martensite, retained austenite (RA), and carbides, arranged in a highly segregated cellular/dendritic solidification structure. The microstructure observed after the tempering treatment of the specimens is tempered martensite, carbides from secondary hardening and a small percentage of retained austenite.

6 REFERENCES

1. Wang, J., Liu, S., Fang, Y. & He, Z. A short review on selective laser melting of H13 steel. *Int. J. Adv. Manuf. Technol.* **108**, 2453–2466 (2020).
2. Lei, F. *et al.* Microstructures and Mechanical Properties of H13 Tool Steel Fabricated by Selective Laser Melting. *Materials* **15**, 2686 (2022).
3. Fonseca, E. B. *et al.* Tempering of an additively manufactured microsegregated hot-work tool steel: A high-temperature synchrotron X-ray diffraction study. *Addit. Manuf.* **55**, 102812 (2022).
4. Looking for high-quality Aluminium Extrusion Die Steel H13! https://www.viratsteel.in/blog/looking-for-high-quality-aluminium-extrusion-die-steel-h13/.
5. Totten, G. E. *Steel Heat Treatment Handbook*. (CRC Press, Boca Raton, Fl, 2007).
6. Haidemenopoulos, G. N. *Physical Metallurgy: Principles and Design*. (Taylor & Francis, a CRC title, part of the Taylor & Francis imprint, a member of the Taylor & Francis Group, the academic division of T&F Informa, plc, Boca Raton, 2018).
7. Gibson, I., Rosen, D., Stucker, B. & Khorasani, M. *Additive Manufacturing Technologies*. (Springer International Publishing, Cham, 2021). doi:10.1007/978-3-030-56127-7.
8. Yap, C. Y. *et al.* Review of selective laser melting: Materials and applications. *Appl. Phys. Rev.* **2**, 041101 (2015).
9. Gao, B., Zhao, H., Peng, L. & Sun, Z. A Review of Research Progress in Selective Laser Melting (SLM). *Micromachines* **14**, 57 (2022).
10. Åsberg, M., Fredriksson, G., Hatami, S., Fredriksson, W. & Krakhmalev, P. Influence of post treatment on microstructure, porosity and mechanical properties of additive manufactured H13 tool steel. *Mater. Sci. Eng. A* **742**, 584–589 (2019).
11. Levy, G. & Wegener, K. 104 PUBLICATIONS 2,048 CITATIONS SEE PROFILE.
12. Spears, T. G. & Gold, S. A. In-process sensing in selective laser melting (SLM) additive manufacturing. *Integrating Mater. Manuf. Innov.* **5**, 16–40 (2016).

13. Bremen, S., Meiners, W. & Diatlov, A. Selective Laser Melting: A manufacturing technology for the future? *Laser Tech. J.* **9**, 33–38 (2012).

14. Véle, F., Ackermann, M., Bittner, V. & Šafka, J. Influence of Selective Laser Melting Technology Process Parameters on Porosity and Hardness of AISI H13 Tool Steel: Statistical Approach. *Materials* **14**, 6052 (2021).

15. Zhang, J., Song, B., Wei, Q., Bourell, D. & Shi, Y. A review of selective laser melting of aluminum alloys: Processing, microstructure, property and developing trends. *J. Mater. Sci. Technol.* **35**, 270–284 (2019).

16. Lee, J. *et al.* Microstructural effects on the tensile and fracture behavior of selective laser melted H13 tool steel under varying conditions. *Mater. Charact.* **155**, 109817 (2019).

17. Lee, J. *et al.* Microstructural effects on the tensile and fracture behavior of selective laser melted H13 tool steel under varying conditions. *Mater. Charact.* **155**, 109817 (2019).

18. Yan, J. J. *et al.* Selective laser melting of H13: microstructure and residual stress. *J. Mater. Sci.* **52**, 12476–12485 (2017).

19. Hanzl, P., Zetek, M., Bakša, T. & Kroupa, T. The Influence of Processing Parameters on the Mechanical Properties of SLM Parts. *Procedia Eng.* **100**, 1405–1413 (2015).

20. Fischer, P. *et al.* Microstructure of near-infrared pulsed laser sintered titanium samples. *Appl. Phys. A* **78**, 1219–1227 (2004).

21. Fischer, P. *et al.* Sintering of commercially pure titanium powder with a Nd:YAG laser source. *Acta Mater.* **51**, 1651–1662 (2003).

22. Mumtaz, K. & Hopkinson, N. Selective laser melting of Inconel 625 using pulse shaping. *Rapid Prototyp. J.* **16**, 248–257 (2010).

23. Buchbinder, D., Schleifenbaum, H., Heidrich, S., Meiners, W. & Bültmann, J. High Power Selective Laser Melting (HP SLM) of Aluminum Parts. *Phys. Procedia* **12**, 271–278 (2011).

24. Mani, M. *et al. Measurement Science Needs for Real-Time Control of Additive Manufacturing Powder Bed Fusion Processes*. NIST IR 8036 https://nvlpubs.nist.gov/nistpubs/ir/2015/NIST.IR.8036.pdf (2015) doi:10.6028/NIST.IR.8036.

25. Yadroitsev, I., Bertrand, Ph. & Smurov, I. Parametric analysis of the selective laser melting process. *Appl. Surf. Sci.* **253**, 8064–8069 (2007).

26. Kurzynowski, T., Chlebus, E., Kuźnicka, B. & Reiner, J. Parameters in selective laser melting for processing metallic powders. in (eds Beyer, E. & Morris, T.) 823914 (San Francisco, California, USA, 2012). doi:10.1117/12.907292.

27. Steen, W. M. & Mazumder, J. *Laser Material Processing*. (Springer London, London, 2010). doi:10.1007/978-1-84996-062-5.

28. Kruth, J. P. *et al.* Selective laser melting of iron-based powder. *J. Mater. Process. Technol.* **149**, 616–622 (2004).

29. Zheng, Z., Sun, B. & Mao, L. Effect of Scanning Strategy on the Manufacturing Quality and Performance of Printed 316L Stainless Steel Using SLM Process. *Materials* **17**, 1189 (2024).

30. Jarfors, A. E. W. *et al.* Build Strategy and Impact Strength of SLM Produced Maraging Steel (1.2709). *Metals* **11**, 51 (2020).

31. Holzweissig, M. J., Taube, A., Brenne, F., Schaper, M. & Niendorf, T. Microstructural Characterization and Mechanical Performance of Hot Work Tool Steel Processed by Selective Laser Melting. *Metall. Mater. Trans. B* **46**, 545–549 (2015).

32. Deirmina, F., Peghini, N., AlMangour, B., Grzesiak, D. & Pellizzari, M. Heat treatment and properties of a hot work tool steel fabricated by additive manufacturing. *Mater. Sci. Eng. A* **753**, 109–121 (2019).

33. Deirmina, F., AlMangour, B., Grzesiak, D. & Pellizzari, M. H13–partially stabilized zirconia nanocomposites fabricated by high-energy mechanical milling and selective laser melting. *Mater. Des.* **146**, 286–297 (2018).

34. Katancik, M., Mirzababaei, S., Ghayoor, M. & Pasebani, S. Selective laser melting and tempering of H13 tool steel for rapid tooling applications. *J. Alloys Compd.* **849**, 156319 (2020).

35. Scipioni Bertoli, U., Wolfer, A. J., Matthews, M. J., Delplanque, J.-P. R. & Schoenung, J. M. On the limitations of Volumetric Energy Density as a design parameter for Selective Laser Melting. *Mater. Des.* **113**, 331–340 (2017).

36. King, W. E. *et al.* Observation of keyhole-mode laser melting in laser powder-bed fusion additive manufacturing. *J. Mater. Process. Technol.* **214**, 2915–2925 (2014).

37. Kaplan, A. A model of deep penetration laser welding based on calculation of the keyhole profile. *J. Phys. Appl. Phys.* **27**, 1805–1814 (1994).

38. DebRoy, T. *et al.* Additive manufacturing of metallic components – Process, structure and properties. *Prog. Mater. Sci.* **92**, 112–224 (2018).

39. Darvish, K., Chen, Z. W. & Pasang, T. Reducing lack of fusion during selective laser melting of CoCrMo alloy: Effect of laser power on geometrical features of tracks. *Mater. Des.* **112**, 357–366 (2016).

40. Duan, C., Zhao, M. & Luo, X. Study on typical defects and cracking characteristics of tool steel fabricated by laser 3D printing. *IOP Conf. Ser. Earth Environ. Sci.* **714**, 032026 (2021).

41. Narvan, M., Al-Rubaie, K. S. & Elbestawi, M. Process-Structure-Property Relationships of AISI H13 Tool Steel Processed with Selective Laser Melting. *Materials* **12**, 2284 (2019).

42. Gu, D. & Shen, Y. Balling phenomena in direct laser sintering of stainless steel powder: Metallurgical mechanisms and control methods. *Mater. Des.* **30**, 2903–2910 (2009).

43. Rahmati, S. & Vahabli, E. Evaluation of analytical modeling for improvement of surface roughness of FDM test part using measurement results. *Int. J. Adv. Manuf. Technol.* **79**, 823–829 (2015).

44. Young, Z. *et al.* Effects of Particle Size Distribution with Efficient Packing on Powder Flowability and Selective Laser Melting Process. *Materials* **15**, 705 (2022).

45. Gao, M., Wang, Z., Li, X. & Zeng, X. The Effect of Deposition Patterns on the Deformation of Substrates During Direct Laser Fabrication. *J. Eng. Mater. Technol.* **135**, 034502 (2013).

46. Holzweissig, M. J., Taube, A., Brenne, F., Schaper, M. & Niendorf, T. Microstructural Characterization and Mechanical Performance of Hot Work Tool Steel Processed by Selective Laser Melting. *Metall. Mater. Trans. B* **46**, 545–549 (2015).

47. Mazur, M., Brincat, P., Leary, M. & Brandt, M. Numerical and experimental evaluation of a conformally cooled H13 steel injection mould manufactured with selective laser melting. *Int. J. Adv. Manuf. Technol.* **93**, 881–900 (2017).